Physics – Uspekhi **66** (3) 288 – 311 (2023)

REVIEWS OF TOPICAL PROBLEMS

PACS numbers: 61.20.Ja, 61.25.Mv, **61.43.–j**

Universal structural properties of three-dimensional and two-dimensional melts

B A Klumov

DOI: https://doi.org/10.3367/UFNe.2022.09.039237

Contents

Abstract. **A brief overview of the key methods for analyzing the structure of three-dimensional (3D) matter is given by using as an example melts of simple model systems like Lennard-Jones, Yukawa, and inverse power law. The behavior of simple structural measures characterizing matter near the melting line is considered in fine detail, and their advantages and disadvantages are discussed. Some indicators that characterize liquid near the melt line are proposed, and their universality and applicability for determining structure of melts of real liquids are discussed. Finally, the structural properties of two-dimensional (2D) liquids are compared with 3D ones. For 2D systems, simple universal criteria of melting are proposed, and their universality is shown using as an example a Yukawa system.**

Keywords: melts, structural properties, local orientational order, rotational invariants, 2D melting, hexatic phase, 2D liquid

1. Introduction

The relationship between the structure of matter and its physical properties is one of the most fundamental problems in condensed matter physics. Significant experimental and computational resources worldwide are used to identify patterns that originate from such a relationship. Such properties of solid materials as strength, viscosity, and brittleness are largely determined by the properties of the short- and medium-range arrangement of atoms in a solid. To date, methods are already available, which enable experimental determination of the positions of individual atoms in amorphous substances (metallic glasses) for several ten thousand particles [1], i.e., solids are being studied at the most detailed level, the level of individual atoms. Such studies are extremely important, since they make it possible to elucidate the influence of the short- and medium-range orientational order on the formation of the amorphous state of matter. For example, it is known that an important role in its formation is played by the icosahedral phase [2], which hinders the crystallization of a system of atoms, a factor of importance for numerous applications.

For liquids, however, such experimental studies will not be available for a long time, and therefore a computational experiment plays an important role in studying such a substance. Due to this, a huge set of atomic configurations requires processing for the determination of the key parameters of the system under study. The examination of the liquid near the melting line is of special importance in these studies. Such liquids or melts often inherit the structural features of the parent crystalline substance. This, in particular, makes it possible to find common structural features in various melts in an attempt to describe them using the universal characteristics of the substance structure.

Such attempts have been made earlier, beginning with the pioneering work of Lindemann [3], who proposed a phenomenological criterion for melting by relating the RMS deviation of an atom to the lattice length. Single-phase melting criteria obtained in the study of the crystal–liquid and liquid–crystal transitions in simple systems are also well known: Hansen–Verlet [4], Raveché [5], etc.

Unfortunately, it turned out that the mentioned criteria are not universal and often vary strongly along the melting line, even within the same system under consideration. Finding universal indicators that characterize a liquid is of importance not only for a liquid near the melting line but also for the entire 'liquid' part of the phase diagram of the substance under study. Recently, the theory of isomorphs has become popular in the description of a liquid [6]. According to this theory, there are lines in the phase diagram along which the thermodynamic properties of the liquid expressed in certain variables are universal. Finding such lines (and one of them is the melting line) and quasi-universal characteristics of the liquid (that vary very weakly along these lines) can greatly reduce the computational resources required to study the properties of the liquid.

B A Klumov
Joint Institute for High Temperatures, Russian Academy of Sciences,
ul. Izhorskaya 13/19, 125412 Moscow, Russian Federation
E-mail: klumov@ihed.ras.ru

Received 30 July 2021, revised 5 July 2022
Uspekhi Fizicheskikh Nauk **193** (3) 305 – 330 (2023)
Translated by M Zh Shmatikov

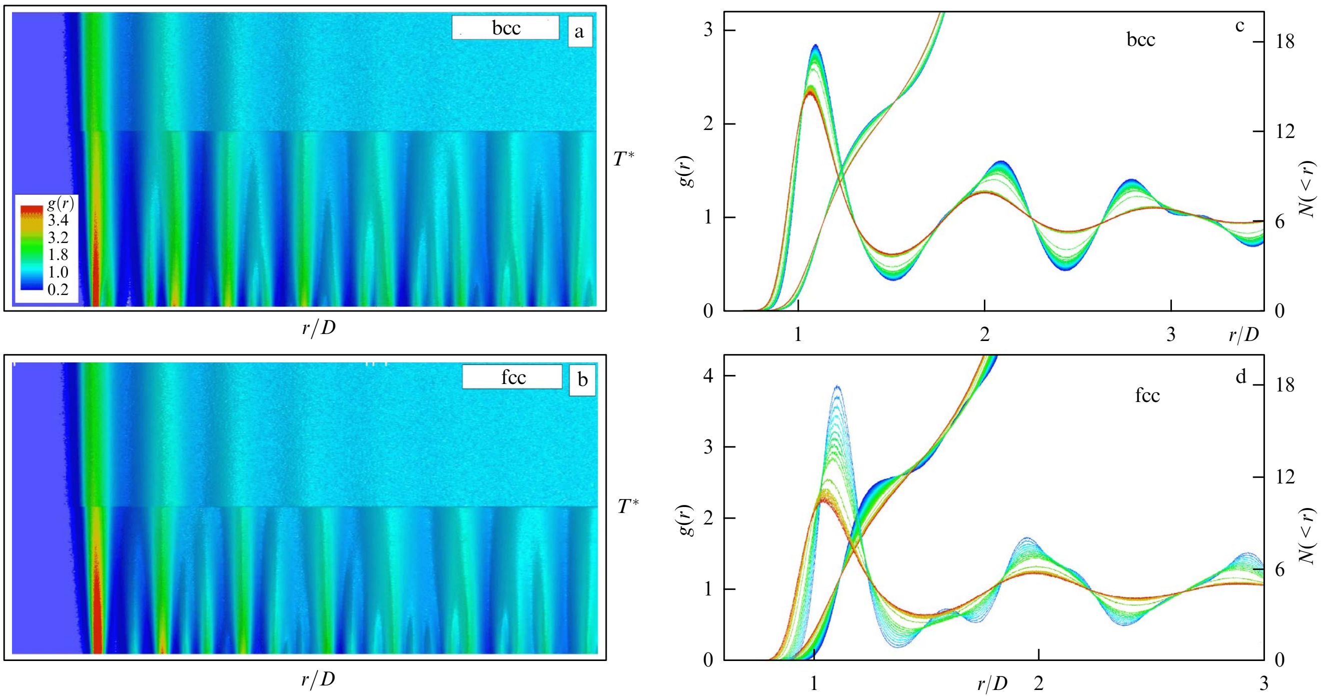

Figure 1. Typical behavior of pair correlation function (PCF) $g(r)$ near the melting region for two types of crystals: (a) bcc and (b) fcc. The 2D PCF is presented as a function of dimensionless distance r/D, where D is the average interparticle distance, and dimensionless temperature T^*. A sharp change in $g(r)$ is observed on all spatial scales and corresponds to the melting of the system. Panels (c) and (d) show the corresponding one-dimensional function $g(r)$ near the crystal–liquid transition. Color of the curves depends on temperature T^* (which increases from blue to red, so blue curves correspond to the heated crystal, and red curves, to the liquid phase). Cumulative functions $N(<r)$ are also displayed, which, in particular, show that, in the case of a bcc melt, the first coordination sphere contains, on average, $N_{\rm nn} \simeq 13$ nearest neighbors. For the fcc melt, a close packing of atoms with $N_{\rm nn} \simeq 12$ is observed.

Presented below is a brief overview of state-of-the-art computational methods for studying the structure of matter using the exploration of melts of a number of simple systems (Lennard-Jones, Yukawa, soft and hard spheres). As an example, well-studied systems such as Lennard-Jones [7, 8], soft spheres [9], and Yukawa [10–12] are considered. Based on their structural characteristics, universal melt indicators are presented. Despite the simplicity of these systems, they are extremely useful in describing real substances, for example, for systems at high pressures and temperatures, when the substance is compressed so strongly that only repulsive forces dominate between the atoms. This, in turn, implies that the interparticle interaction can be described by repulsive potentials such as soft spheres or Yukawa (Debye–Hückel).

Below, unless stated otherwise, the main tool for obtaining atomic configurations is the method of classical molecular dynamics implemented for a canonical ensemble with a Nose–Hoover thermostat (NVT) and periodic boundary conditions [13]. The typical number of particles N in the systems under study varied within the range $N \sim 10^4 - 10^6$, which practically makes it possible to rule out the influence of the system size on the resulting configurations.

2. Melts of three-dimensional systems and their structural features

2.1 Pair correlation functions of melts of simple systems

The simplest characteristics of the structure of an ensemble of particles is a two-point spatial correlator that describes the translational order in the system under study — the pair correlation function (PCF) $g(r)$, which is determined for three-dimensional systems by the formula

$$g(r) = \frac{L^3}{N^2} \left\langle \sum_i^N \sum_{j \neq i}^N \delta(\mathbf{r} - \mathbf{r}_{ij}) \right\rangle , \qquad (1)$$

where N/L^3 is the density of particles in the system and r_{ij} is the distance between particles i and j. Another characteristic is the so-called cumulative PCF, the function $N(<r)$, generated by the pair correlation function,

$$N(<r) \equiv \int_0^r 4\pi r^2 g(r)\, \mathrm{d}r , \qquad (2)$$

which determines the average number of particles in a sphere of radius r. The cumulative function $N(<r)$ can be used to easily calculate the average number of nearest neighbors $N_{\rm nn}$ in the first coordination sphere (the radius of which is usually set by the distance to the first nonzero PCF minimum) and, consequently, determine an important characteristic of the system, its packing density. For close-packed systems, $N_{\rm nn} = 12$. The function $g(r)$ describes the density distribution in the vicinity of the central particle and, for a liquid, it usually exhibits several peaks that diminish with increasing distance r, which reflects a decrease in spatial correlations. For a liquid at $r \gg D$, where D is the average distance between particles, $g(r) \to 1$. For the gas phase, the function $g(r) = 1$ on all but the smallest spatial scales.

Figure 1 shows as an example the characteristic pair correlation functions $g(r)$ as a function of temperature T^* obtained in the heating and subsequent melting of two widespread types of crystal lattices: bcc (body-centered cubic) (displayed in Fig. 1a, c) and fcc (face-centered cubic) (displayed in Fig. 1b, d). Figures 1c, d show the one-dimensional dependences $g(r)$ and $N(<r)$ near the region of crystal–liquid transition. The color of each curve, which corresponds to the temperature of the system, changes from blue (hot crystal) to red (liquid) as the temperature rises.

To reveal the subtle details of the change in PCF and the cumulative function $N(<r)$, the equilibrium configurations of atoms upon heating were calculated using a small temperature step $\delta \simeq 0.01 T_{\rm m}$, where $T_{\rm m}$ is the melting temperature of each of the considered systems. This made it possible to obtain detailed information on the form of these functions near the crystal–liquid transition. It is clearly seen, for example, that in the process of melting the function $g(r)$ undergoes a sharp change on all spatial scales in both cases, and near the line of transition from the side of the solid phases, the characteristic fine details of the crystal lattice are largely lost.

Analyzing the cumulative functions $N(<r)$ and $g(r)$, it can be easily shown that in the case of a bcc melt the average number of nearest neighbors in the first coordination sphere is $N_{\rm nn} \simeq 13$ (Fig. 1a); a consequence of thermal smearing of the second coordination shell and its partial association with the first one. It should be recalled that the second shell of an ideal bcc crystal consists of six atoms (the first shell contains eight atoms located at the cube vertices) and is close (at a distance of $\sqrt{4/3}D \simeq 1.15D$) to the first coordination shell. When heated, they partially combine. This effect is also observed in the region of the heated crystal near the melting line (as evidenced by the form of the function $g(r)$ shown in Fig. 1a).

Such a feature of the crystal lattice hinders identification of bcc-like crystallites in natural and numerical experiments related, for example, to the crystallization of colloidal and complex plasma, the formation of metallic glasses from a melt, etc.

In the case of melting an fcc crystal, the melt is close packed and $N_{\rm nn} \simeq 12$. This important observation will be needed later in the analysis of the angular characteristics of the nearest neighbors.

Since the destruction of the translational order during the melting of a substance occurs on all spatial scales, it is quite natural to use for the quantitative description of the pair correlation function $g(r)$ its simplest properties. They are, first of all, the characteristics of the first coordination sphere, namely the magnitude of the first PCF peak — the parameter $g_{\max}$ — and the value of the first nonzero PCF minimum — the parameter $g_{\min}$. The importance of these parameters will be demonstrated below. It should be noted that quite often their ratio, the parameter $R \equiv g_{\min}/g_{\max}$ [5], or its inverse value $1/R$ is used as the simplest indicator of structural transitions in a substance. For example, for the Lennard-Jones (LJ) system with potential $U_{\rm LJ}(r)$, which, in dimensionless form, is

$$U_{\rm LJ}(r) = 4\left(\frac{1}{r^{12}} - \frac{1}{r^6}\right), \qquad (3)$$

it has been shown in [5] that $R \simeq 0.2$ near the melting line on the liquid side. This parameter has also been repeatedly used as an indicator of crystallization and glass transition of various systems (for example, [14]). We show below that the separate use of the $g_{\max}$ and $g_{\min}$ parameters provides much more information about the system under study.

Figure 2 shows the behavior of the PCF-associated structural indicators considered above, the parameters $g_{\max}$, $g_{\min}$, and $1/R$, during the melting of a Lennard-Jones system. These parameters are presented as a function of the dimensionless temperature (normalized to the melting point $T_{\rm m}$) for three values of the dimensionless density ρ^* of the LJ system. The chosen values of ρ^* span a wide range of melting temperatures, which change by two orders of magnitude when the density is tripled: from $T^* \simeq 1$ for $\rho^* = 1$ to $T^* \simeq 200$ for $\rho^* = 3.5$.

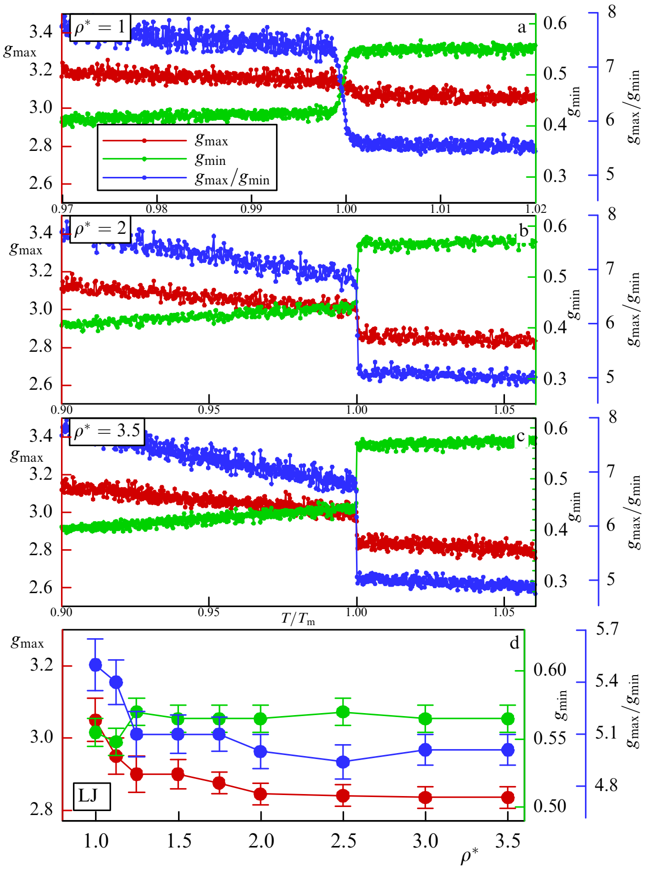

Figure 2. Melting of the Lennard-Jones system: behavior of PCF-associated structural indicators near the crystal–liquid transition line. Parameters $g_{\max}$, $g_{\min}$, and $1/R = g_{\max}/g_{\min}$ are presented as functions of the reduced temperature (normalized to the melting temperature) for three values of the system's dimensionless density: $\rho^* = 1$ (a), $\rho^* = 2$ (b), and $\rho^* = 3.5$ (c). The ρ^* values chosen cover a wide range of Lennard-Jones T^* melting temperatures (which range from $T^* \simeq 1$ at $\rho^* = 1$ to $T^* \simeq 200$ at $\rho^* = 3.5$). A sharp change in all considered parameters can be clearly seen in the melting region of the system. Panel (d) shows the dependence of these parameters, determined for a liquid near the melting curve, on density ρ^*. Almost universal behavior is exhibited by only the $g_{\min}$ parameter; remaining parameters change significantly when the density of the system changes.

It can be seen that all of these structural parameters undergo a sharp jump when the Lennard-Jones system melts; however, the parameter $g_{\min}$ alone can be considered quasi-universal, since it does not really depend on the density of the system in the considered range of its variation. Other parameters change noticeably with density, both in the crystalline and in the liquid phase. For an LJ melt, this is illustrated in Fig. 2d, where these parameters are plotted as functions of density. The increase in the peak $g(r)$ with decreasing density ρ^* can be explained by the fact that for high values of ρ^* the repulsive term of the pairwise interaction of atoms, proportional to r^{-12}, plays a dominant role in the formation of the short-range order, while, as the density

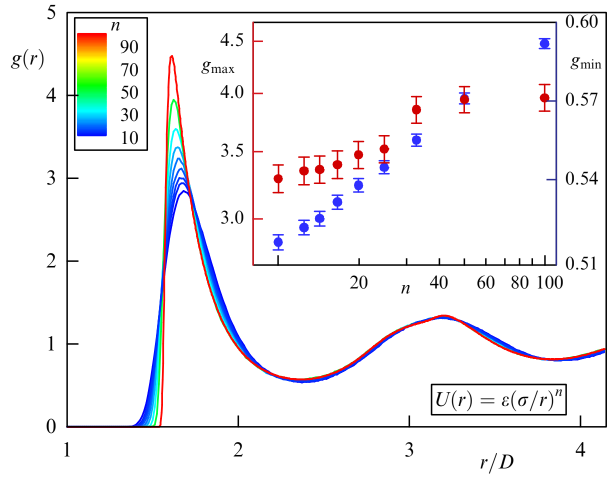

Figure 3. Pair correlation functions $g(r)$ calculated for a system melt with an inverse power-law repulsion for various values of the exponent n [18]. Color of the curves, which depends on parameter n, changes from blue to red as it increases from $n = 10$ to $n = 100$ spanning a wide range of pair interaction softness: from soft ($n \sim 10$) to hard ($n \sim 100$) spheres. Inset shows the behavior of $g_{\max}$ (blue symbols) and $g_{\min}$ (red symbols) parameters depending on parameter n. It is clearly seen that, with increasing interaction softness (parameter n), the peak of the pair correlation function monotonically increases, and the value of the PCF peak is uniquely determined by the value of exponent n. Indicator $g_{\min}$ changes very little within the specified interaction softness limits and thus exhibits almost universal behavior.

diminishes, attraction, which decreases as $\propto r^{-6}$, starts being effective. The crossover between these two modes is observed at $\rho^* \simeq 1.5$.

This leads to an important conclusion: the value of the first PCF $g_{\max}$ peak is a very important characteristic of the melt, since it is determined by the softness (or hardness) of the pairwise interaction of atoms. This is also true of real substances, since it is known that the properties of a liquid on the melting line are largely determined by the pairwise interaction of atoms [15, 16]. To confirm this conclusion, in Fig. 3, the pair correlation functions are displayed for the melts of a system of soft spheres, inverse power law (IPL) systems, with a pairwise interaction potential given by

$$U_{\mathrm{IPL}}(r) \propto \frac{1}{r^n} \,. \tag{4}$$

Such systems have been fairly well studied (see, for example, [9–17]), and their phase state is determined by only one parameter: the exponent of the power of interaction n. Figure 3 shows pair correlation functions $g(r)$ for melts of soft-sphere systems calculated for various values of n starting from $n = 10$ and above, which span a wide range of softness/softness of interparticle interaction from soft ($n \simeq 10$) to hard ($n \simeq 100$) spheres [18]. The inset in Fig. 3 presents how parameters $g_{\max}$ and $g_{\min}$ depend on the value of n. It clearly shows that, with an increase in the softness of the pair interaction (it is convenient to use parameter n as a characteristic), parameter $g_{\max}$ constantly grows, and its value is uniquely determined by the value of parameter n. However, the parameter is $g_{\min} \simeq 0.55$ and changes very weakly within the considered limits of the variation in the exponent n, i.e., is a virtually universal characteristic of the melt of a system of soft spheres. We also note a very weak variation in the magnitude of the second PCF peak in soft sphere melts.

Due to this, parameters $g_{\max}$ and $g_{\min}$ are simple, reliable, and extremely useful characteristics of a liquid. The parameter $g_{\min}$, being almost universal, makes it possible to determine how far the investigated liquid is from the melting curve of a substance, while parameter $g_{\max}$ provides an estimate of the softness/softness of the pair interaction in the melt.

It is worth mentioning that, to describe the structure of a three-dimensional fluid, such integral PCF characteristics are used as the pair entropy s,

$$s_2 = -2\pi\rho \int \Big(g(r) \ln \big(g(r)\big) - g(r) + 1 \Big)\, r^2 \,\mathrm{d}r \,, \tag{5}$$

or static structure factor $S(k)$,

$$S(\mathbf{k}) = 1 + \rho \int \mathrm{d}\mathbf{r}\, g(\mathbf{r}) \exp\left(i\mathbf{k}\mathbf{r}\right), \tag{6}$$

which can be simplified for an isotropic and homogeneous fluid to

$$S(k) = 1 + 4\pi\rho \int_0^\infty \mathrm{d}r \,\big(g(r) - 1\big)\, r^2 \,\frac{\sin(kr)}{kr} \,. \tag{7}$$

It can be shown, however, that their behavior exhibits the same regularities that have already been revealed in the behavior of parameter $g_{\max}$ depending on the softness of the interparticle interaction, and, in the context of this section, their study does not add new information to that already obtained (despite the fact that, for example, the static structure factor $S(k)$ is one of the main experimentally obtained characteristics of condensed matter, from which the pair correlation function $g(r)$ is determined by means of the inverse Fourier transform).

It should be noted that all the presented dependences $g(r)$ for melts of soft spheres (as can be clearly seen in Fig. 3) differ for different n only within the limits of the first coordination sphere; for large $r > D$, all pair correlation functions of the melts virtually coincide. The same is observed for the Lennard-Jones system (for various density values ρ^*) and for the Yukawa system (for various values of the screening parameter κ; see the discussion below).

This implies that the integral characteristics of the PCF, for example, the pair entropy s_2 or the static structure factor $S(k)$, only mask the important dependence of the first PCF peak on the softness of the interparticle interaction (while remaining important characteristics of the structure of matter). Many thermodynamic functions (for example, pressure and internal energy) depend on the function $g(r)$ in an integral way and, since it changes noticeably only within the first coordination sphere along certain lines of the phase diagram (and not the melting line alone). Owing to this, the theory of isomorphs in the description of a liquid has gained popularity [19–27], according to which the thermodynamic functions along certain lines of the phase diagram with a certain normalization are the same. Such a description can greatly reduce the computational and experimental resources required for exploring the phase diagram of a liquid for the substance under study.

It is also of interest to trace the behavior of the parameter $g_{\max}$ for a system of soft spheres in the region of exponent $n < 10$, where, in particular, the structural transition of the solid phase from fcc to bcc occurs (which is observed at $n \simeq 6$ [24]). These data are shown in Fig. 4, where, for comparison,

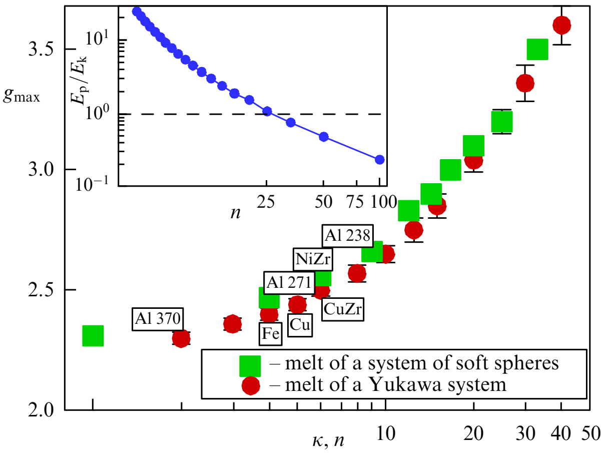

Figure 4. Melts of soft sphere and Yukawa systems. Dependences of parameter $g_{\max}$ on exponent n and screening parameter κ are shown in a wide range of softness values of the interparticle interaction. Additionally, data are given for some melts of real substances, including multicomponent systems. In the case of an aluminum melt, the data of quantum mechanical calculations [39] are presented as obtained for various densities of aluminum (2.38, 2.71, and 3.7 g cm^{-3}; the values are indicated on the plot). Calculated data exhibit an interesting effect: as density increases, the interaction between particles in liquid aluminum becomes significantly softer. Another interesting effect is connected with the behavior of coupling parameter Γ, which characterizes the nonideality of a system of interacting particles, as a function of n ($\Gamma \equiv E_p/E_k$, where E_p and E_k are potential and kinetic energies of the system). Such dependence $\Gamma_m(n)$ for melts of soft spheres is shown in the inset. It can be seen that for $n > 25$ coupling parameter Γ_m becomes less than one. In particular, this implies that such melts are a new and interesting state of matter: strongly correlated but weakly coupled systems [24–26]. This greatly distinguishes them from ordinary melts, which usually are strongly correlated and strongly coupled

the results calculated for the melt of a Yukawa (or Debye–Hückel) system, a system with a repulsive potential, are displayed:

$$U(r) = \frac{Q}{r} \exp\left(-\frac{r}{\lambda}\right), \qquad (8)$$

where Q is the particle charge, and λ is the screening length considered for various values of the screening parameter $\kappa \equiv D/\lambda$, where D is the average distance between particles in the system.

The Yukawa system, which has been actively studied in recent years, in particular, in connection with the discovery of plasma crystals, is an important model system for studying complex (dusty) plasma [28–38], a highly nonideal system of charged micron-size particles located in gas discharge plasma. The melting and crystallization of such a plasma were studied, notably, at the Mir International Space Station [36, 37].

The Yukawa system has much in common with the system of soft spheres. For example, for small values of the parameter κ, this system at low temperatures also has a bcc lattice. Similarly to the soft sphere system, the Yukawa system exhibits a solid-state transition from bcc to fcc at certain values of the screening parameter κ, so their comparison is extremely useful. Figure 4 shows the dependences of the parameters $g_{\max}(n)$ and $g_{\max}(\kappa)$ calculated on the melting line for the soft sphere and Yukawa systems. It is clearly seen that these parameters differ slightly for these two systems, and a monotonic increase in parameter $g_{\max}$ is observed with an increase in the softness of the pair interaction. Based on these results, it should be expected that at least the melts of these systems will feature similar physical properties.

Additionally, Fig. 4 shows data for some melts of real substances. In the case of an aluminum melt, the results of quantum mechanical calculations [39] are presented for various aluminum densities (2.38, 2.71, and 3.7 g cm^{-3}, respectively), which exhibit an interesting effect: with increasing density, the interparticle interaction in liquid aluminum gets increasingly softer, which, apparently, implies an enhanced contribution of electrons during the interaction of aluminum ions in its melt.

Another interesting effect shown in the inset to Fig. 4 is associated with the parameter Γ, which is a characteristic of the nonideality of the melt, at different values of the exponent n. Here, $\Gamma \equiv E_p/E_k$, where E_p and E_k are the potential and kinetic energies of the system, respectively. This dependence is shown by the blue line in the inset to Fig. 4. Melts of a substance are usually strongly coupled systems, in which the coupling parameter Γ_m noticeably exceeds unity: $\Gamma_m \gg 1$. It is also clearly seen here that Γ_m greatly decreases with an increase in exponent n, and for $n > 25$ the coupling parameter Γ_m becomes less than unity. This implies that such melts are a rather exotic state of the matter's strongly correlated but weakly coupled liquid [18, 26]. Examination of such objects is of utmost interest. It can also be shown that for $n > 25$ a weakly coupled system (with parameter $\Gamma < 1$) is not only a liquid on the melting line but also a crystal near the melting line due to the fact that, during the crystal–liquid transition at the specified values of parameter n, there is virtually no jump in the values of E_p and E_k, which is observed at small values of n. This implies, for a crystal on the melting line at $n > 25$, that the dependence $\Gamma^{\text{cr}}(n)$ virtually coincides with $\Gamma^{\text{melt}}(n)$ of the melt: $\Gamma^{\text{cr}}(n) \approx \Gamma^{\text{melt}}(n)$. Of course, all of the above is also true for the Yukawa system for values of the screening parameter $\kappa > 25$.

The data shown in Fig. 4 make it possible to establish a direct correspondence between melts of real substances and their IPL and/or Yukawa-like counterparts. In this case, it is sufficient to use only one parameter, the peak of the pair correlation function $g_{\max}$. The availability for real melts of IPL or Yukawa-like analogs is very important for a comparative study of their general physical properties. This is especially interesting for real liquids at high densities and pressures, when the substance is compressed so strongly that attraction disappears in the interparticle interaction and the repulsive part dominates, which can always be expressed in terms of power and/or exponential functions, i.e., such a substance is an IPL or Yukawa-like one.

It has been found recently in [38] that, for a 3D Yukawa fluid system, the parameters $g_{\min}$ and the reduced parameter $g^*_{\max} \equiv g_{\max}(T)/g_{\max}(T_m)$, where T is the temperature of the liquid under study and T_m is the melting temperature, do not really depend on the screening parameter κ, but only depend on the value of the inverse reduced temperature T_m/T. This conclusion is illustrated in Fig. 5, which shows the behavior of the described characteristics of liquid as functions of the parameter T_m/T for two values of the screening parameter ($\kappa = 1$ and $\kappa = 4$). It can be seen that the considered parameters are virtually independent of the value of κ, i.e., they are universal characteristics of a Yukawa liquid, and their values are only determined by the value of the parameter T_m/T. This makes it easy to determine the place of the investigated Yukawa fluid in the phase diagram, i.e., to determine the values of κ and T using only the characteristics

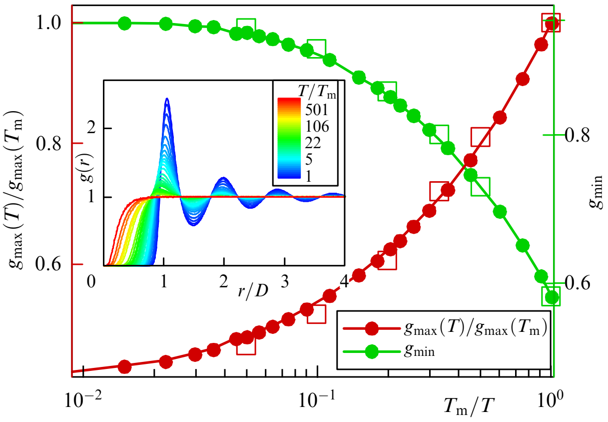

Figure 5. Three-dimensional Yukawa liquid system. Behavior of parameters $g_{\min}(T_{\mathrm{m}}/T)$ (green symbols) and $g^*_{\max} \equiv g_{\max}(T)/g_{\max}(T_{\mathrm{m}})$ (red symbols) as a function of reciprocal normalized temperature T_{m}/T for two values of the screening parameter is shown: $\kappa = 1$ (curves) and $\kappa = 4$ (unfilled squares). It can be seen that the considered parameters exhibit the universal behavior of a Yukawa liquid in a wide temperature range ($T/T_{\mathrm{m}} \sim 1-100$). Inset shows the variation in the pair correlation functions of a Yukawa liquid at these temperatures. Color of curves $g(r)$ depends on parameter T_{m}/T and changes with its growth from blue to red.

of the pair correlation function; this is extremely important, for example, in experiments with complex and colloidal plasmas, which are often Yukawa-like systems.

2.2 Voronoi method

An important method for determining the structural properties of disordered media is the method of Voronoi polyhedra or VT (Voronoi Tessellation) [40], which is widely used in condensed matter physics to analyze the local structure of a substance (for example, [41, 42]) and determine the topology of liquid and crystalline clusters in studying short-range order in metallic glasses [43–47]. The great advantage of the VT method is that it does not contain any additional parameters (parameter-free method) and is almost uniquely determined by the given arrangement of atoms in three-dimensional space. Space is partitioned into convex polyhedra, and each such polyhedron is associated with a certain cluster of atoms. For 3D and 2D systems, the Voronoi partition is a nontrivial geometric problem, but one that has already been solved.

Voronoi polyhedra are obtained as a result of planes that intersect at right angles the midpoints of segments connecting the central atom of the cluster with its nearest neighbors, in such a way that the resulting polyhedron is convex [42]. Such a construction determines, in particular, the number of nearest neighbors for each particle N_{VT} which, naturally, by construction coincides with the number of faces of the Voronoi polyhedron. A serious disadvantage of the VT method (discussed below) is that the method under consideration usually overestimates the number of nearest neighbors, atoms from the second coordination sphere often being included in the Voronoi polyhedron.

The topology of such a polyhedron (sometimes referred to as a Voronoi polyhedron) is defined in the VT method by Voronoi indices $\langle n_3, n_4, n_5, n_6\rangle$, where n_i is equal to the number of faces in the constructed polyhedron with sides 3, 4, 5, and 6, respectively (more indices can be used, for example, n_7, n_8, etc.; however, such polyhedra appear due to very strongly distorted clusters, which are quite rare and hardly make any contribution to the structural properties of the liquid). The number of nearest neighbors N_{VT} in the VT method is equal to the sum of the Voronoi indices: $N_{\mathrm{VT}} \equiv \sum n_i$.

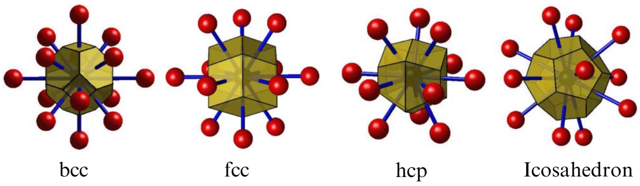

Figure 6. Ideal crystal structures and their Voronoi polyhedra. Shown are clusters consisting of a central atom and its nearest neighbors, as well as the corresponding Voronoi polyhedra. Shown from left to right are bcc clusters (with Voronoi indices $\langle 0,6,0,8\rangle$), fcc ($\langle 0,12,0,0\rangle$), hcp (hexagonal close packing) ($\langle 0,12,0,0\rangle$), and the icosahedral phase (ico) ($\langle 0,0,12,0\rangle$), respectively. It can be seen that, for the bcc lattice, the Voronoi partition includes atoms from the second coordination sphere. It is also seen that the topologies of the fcc and hcp lattices characterized by the Voronoi indices coincide.

Figure 6 shows several ideal crystalline clusters and their corresponding Voronoi polyhedra. Shown from left to right are bcc clusters (with Voronoi indices $\langle 0,6,0,8\rangle$ and $N_{\mathrm{VT}} = 14$), densely packed lattices: fcc ($\langle 0,12,0,0\rangle$ with $N_{\mathrm{VT}} = 12$) and hcp (hexagonal dense packing) ($\langle 0,12,0,0\rangle$ with $N_{\mathrm{VT}} = 12$), and the icosahedral phase (with Voronoi indices $\langle 0,0,12,0\rangle$ and $N_{\mathrm{VT}} = 12$).

The example of fcc and hcp lattices, which have the same Voronoi indices, shows that such indices do not completely describe the topology of even an ideal crystalline cluster and, therefore, their use is limited. For certain types of symmetry [48, 49], even insignificant distortions of the positions of atoms in a crystal radically change its Voronoi indices and, consequently, the number of nearest neighbors determined by the VT method. From a geometric perspective, this implies the appearance of small faces in the Voronoi polyhedron, which correspond to distant nearest neighbors. The consideration of ideal clusters above shows that the fcc and hcp lattices turn out to be unstable with respect to the Voronoi partitioning and the formation of small faces, while the bcc lattice and the icosahedral phase are fairly stable with respect to minor displacements of atoms. This circumstance, notably, predetermined the wide use of the Voronoi method in the physics of supercooled liquids and metallic glasses (see, for example, [47, 50]), since their physical and structural properties are largely specified by clusters with icosahedral symmetry [51, 52], which are quite easily determined by the Voronoi method even for multicomponent systems.

Figure 7 considers the bcc and fcc lattices near the melting line from the side of the crystal and presents the topological properties of the corresponding solid-state clusters obtained by the Voronoi partitioning method. The most common topological structures for both types of lattice are displayed. It can be seen that the heated bcc lattice retains the topological features of an ideal crystal, since it contains a significant number of clusters with the topology $\langle 0,6,0,8\rangle$. In the case of the fcc lattice, this is not the case, and it can be shown that the fraction of clusters with Voronoi indices $\langle 0,12,0,0\rangle$ is very small, $\leqslant 0.01$. It should be noted that the same effect is also observed for the hcp crystal near its melting line.

Thus, heated close-packed (fcc and hcp) crystals almost completely lack the topological features of an ideal crystal. Due to the instability of a number of ideal and distorted

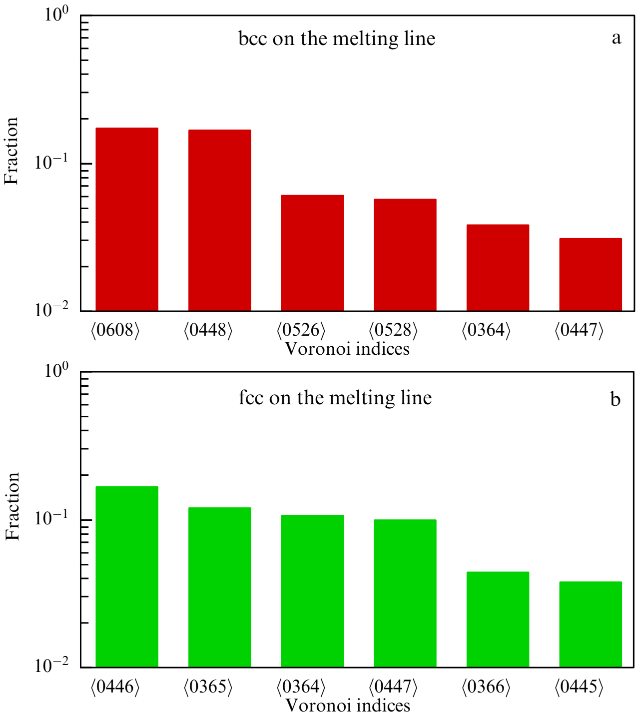

Figure 7. Fraction of the most common solid-state clusters and their Voronoi indices on the melting line of bcc (a) and fcc (b) crystals. It can be seen that the heated bcc lattice retains the topological features of an ideal crystal, since it contains a significant number of clusters with the topology $\langle 0,6,0,8\rangle$. A heated fcc crystal, however, exhibits virtually no such features: fraction of clusters with Voronoi indices $\langle 0,12,0,0\rangle$ is very small, $\leqslant 0.01$.

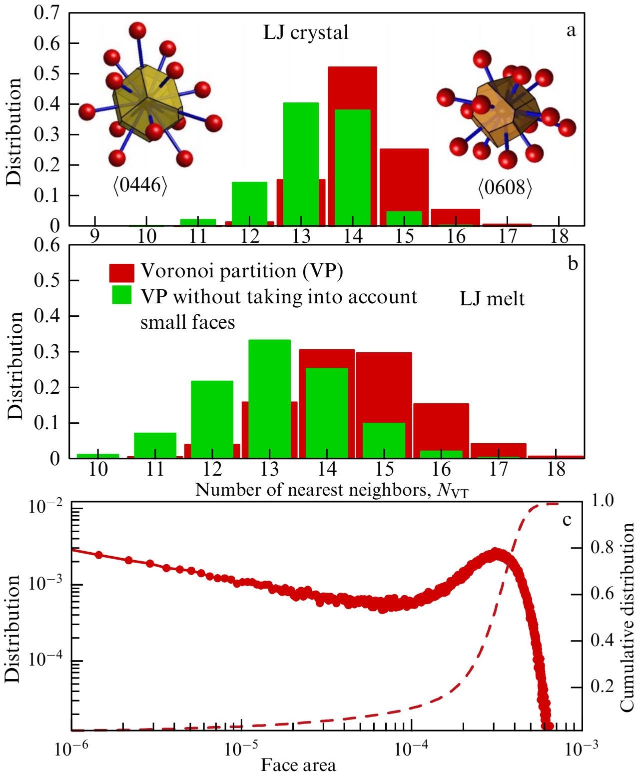

Figure 8. Distribution of the number of nearest neighbors $N_{\rm VT}$ near the melting line of a Lennard-Jones system. (a) Heated fcc crystal, (b) melt. Nearest neighbors were determined from Voronoi partitioning with removal (green) and without removal (red) from the Voronoi polyhedron of small faces, which emerge due to distant atoms. Faces with an area less than 0.1 of the average face area in Voronoi polyhedra were removed. One can clearly see a noticeable shift in the distribution to the region of smaller $N_{\rm VT}$ for both a crystal and a melt. (c) Distribution of faces in the LJ melt depending on their area, as well as its cumulative characteristic, which can be used to easily determine the fraction of particles with small faces. Inserts in panel (a) shows distorted fcc (left) and bcc (right) crystal clusters, the corresponding Voronoi polyhedral, and their indices. Instability with respect to the formation of small faces in the distorted fcc cluster and the relative stability of the bcc-like cluster are seen.

lattices with respect to Voronoi partitioning, the central particle of the crystalline cluster acquires additional nearest neighbors, which correspond to faces of the Voronoi polyhedron with a relatively small area. The same situation occurs in liquid clusters. This implies that the Voronoi method overestimates the number of nearest neighbors in a substance, which results in significant errors in determining its structure using this method (see, for example, [53]).

As an example, Fig. 8 shows how the distribution of the number of nearest neighbors $N_{\rm VT}$ changes if small faces (and, consequently, distant particles resting on such faces) are removed from the Voronoi polyhedron. The Lennard-Jones system for the fcc crystal (Fig. 8a) and melt (Fig. 8b) near the melting line is considered. Here, faces with an area of less than 0.1 of the average face area in the Voronoi polyhedron were removed. A significant shift of the distribution to the region of smaller $N_{\rm VT}$ values is clearly seen for both the crystal and the melt. The distribution of the number of nearest neighbors becomes close to that obtained by standard methods, for example, using the SANN algorithm [54]. The introduction of a cutoff of small faces in the Voronoi method implies the introduction of a parameter, which certainly reduces the value of the method.

Figure 8c shows the distribution by area of Voronoi polyhedron faces in the melt of the Lennard-Jones system and the cumulative characteristic of this distribution, which makes it easy to estimate the fraction of particles with small faces. For the case of the LJ melt considered above, the proportion of such particles is about 10%. Insets in Fig. 8a show distorted fcc (left) and bcc (right) crystal clusters and the corresponding Voronoi polyhedra and their indices. One can see the instability to the formation of small faces in the distorted fcc-like cluster and the relative stability of the bcc-like cluster.

It is worth noting that the shape of clusters with the same Voronoi indices can differ greatly, even for crystallites stable to the appearance of small faces. For example, clusters with Voronoi indices $\langle 0,0,12,0\rangle$, i.e., clusters with pentagonal symmetry of the Voronoi polyhedron faces and dense packing, are commonly considered icosahedral, despite their possible strong difference in shape from the ideal icosahedron [44].

The same, but to an even greater extent, applies to clusters in a liquid. For example, it can be shown that, in an LJ melt, the most common clusters are those with Voronoi indices $\langle 0,3,6,4\rangle$, $\langle 0,2,8,4\rangle$, $\langle 0,3,6,5\rangle$, etc. The topology of such clusters is extremely sensitive to displacements of nearest neighbors, and, to describe them, methods are required that are much less sensitive to such displacements. These methods are based on the description of the short-range order for each particle using the angular characteristics of the nearest neighbors. The applicability of the Voronoi method to the description of liquid and distorted crystalline clusters (with rare exceptions) is rather limited; it is recommended to

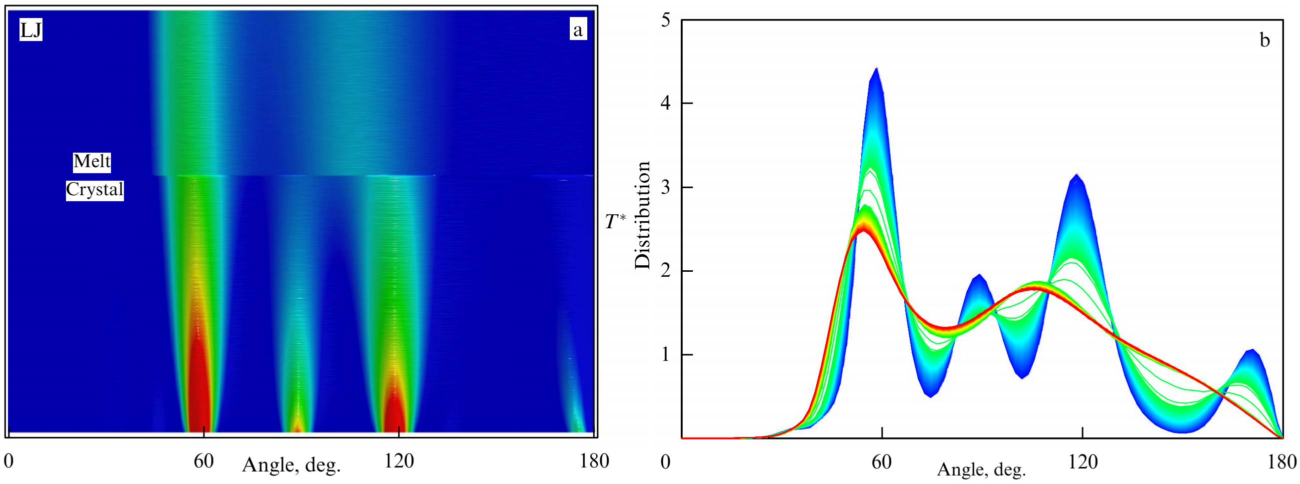

Figure 9. Behavior of function $P(\theta)$ in the process of melting of a Lennard-Jones system. (a) Two-dimensional dependence of the BADF on angle θ and temperature of the system T^* near the melting line. Value of a two-dimensional function is indicated by color and increases from blue to red. A sharp change in $P(\theta)$ corresponds to melting of the system and destruction of local orientational order (melting line is shown in the figure). (b) One-dimensional dependences $P(\theta)$ at various temperatures plotted with the same small step δT in temperature: $\delta T \simeq 10^{-2} T_{\mathrm{m}}$, where T_{m} is the melting temperature of the system. Color of one-dimensional curves depends on temperature and changes from blue to red as it increases. Blue curves correspond to the fcc crystal, and red curves correspond to liquids near the melting line. Similarly to the 2D case, the crystal–liquid transition is clearly seen, accompanied by a sharp decrease in the first BADF peak and a change in the shape of function $P(\theta)$, in which, in particular, the distribution peaks at angles $\theta \simeq \pi$ and $\theta \simeq \pi/2$ disappear. Distribution $P(\theta)$ was calculated taking into account 12 nearest neighbors in the approximation of close packing of atoms.

combine it with other methods, primarily, with those describing the local orientational order [48–52]. We consider below such a combination of two approaches to studying the structure of a Lennard-Jones melt. In conclusion, we note that the Voronoi method can be successfully used in the study of so-called empty liquids, since cavities in such systems can be identified using this method quite easily (see, for example, [55]).

2.3 Local orientational order in melts

To analyze the local orientational order in a system of atoms, we first consider the behavior of a simple angular three-point correlator — the function of the angular distribution of nearest neighbors with respect to the central atom, or the bond angle distribution function (BADF) [7]:

$$P(\theta) = \frac{1}{N n_{\mathrm{nn}}(n_{\mathrm{nn}} - 1)} \left\langle \sum_{k=1}^{N} \sum_{i=1}^{n_{\mathrm{nn}}} \sum_{j \neq i}^{n_{\mathrm{nn}}-1} \delta(\theta - \theta_{ikj}) \right\rangle . \qquad (9)$$

Here, the summation is carried out for all N particles in the system and over all pairs i, j of nearest neighbors n_{nn} (for which the angle θ_{ikj} between them with respect to the central particle k is calculated). Thus, the distribution $P(\theta)$, which determines the probability of two nearest neighbors forming an angle θ between themselves and the central particle, is an important characteristic of the local orientational order.

Figure 9 shows, as an example, the melting of a Lennard-Jones system in terms of the behavior of the BADF distribution. The two-dimensional dependence of the BADF on the angle θ and temperature of the system T^* near the melting line is shown. The value of the 2D function shown in color increases from blue to red. The $P(\theta)$ distribution peaks in the crystalline phase are clearly visible, corresponding to the arrangement of atoms in the fcc lattice. The distribution $P(\theta)$ was calculated taking into account 12 nearest neighbors for each particle, which is justified due to the close packing of the system. A sharp change in $P(\theta)$ corresponds to the melting of the system and the destruction of the local orientational order. The crystal–liquid transition line is clearly seen in this figure. The one-dimensional dependences $P(\theta)$ at various temperatures are shown on the right, plotted with the same temperature step $\delta T^* \simeq 0.01 T_{\mathrm{m}}$, where T_{m} is the melting temperature of the LJ system. The color of the curves, which depends on the temperature, changes from blue to red as the temperature increases. The blue curves in the inset correspond to the fcc crystal, while the red curves, to the liquid. Similarly to the 2D case, the crystal–liquid transition is clearly visible, accompanied by a sharp decrease in the first BADF peak and a change in the shape of the function $P(\theta)$, in which, in particular, the distribution peaks at angles $\theta \simeq \pi$ and $\theta \simeq \pi/2$ disappear. Thus, the BADF distribution makes it possible to immediately distinguish in a qualitative and quantitative way a heated crystal from its melt

Note that it is quite difficult to determine the crystal structure based on the shape of the BADF distribution, since many types of lattices have peaks in the same range of angles θ. The thermal broadening of such distributions only complicates the problem. If, however, a melt is being studied, the situation is different: simple liquids are characterized by the presence of two maxima in the $P(\theta)$ distribution, which are observed at $\theta \simeq 56°$ for the first peak and at $\theta \simeq 108°$ for the second. As the liquid temperature increases, both peaks broaden, and their values decrease. As in the case of the pair correlation function $g(r)$, it is of importance to find out to what extent the BADF function is universal for the melt of a substance and whether it can be used (in particular, the values of the two indicated maxima of the $P(\theta)$ distribution) to construct simple melting indicators.

Figure 10 shows dependences $P(\theta)$ for melts of the system with inverse power-law repulsion in a range of values of the exponent n from 10 to 50, which spans a wide range of interparticle interaction softness (from soft to hard spheres). It can be seen that the dependence $P(\theta)$ is rather weakly affected by the softness of the interaction potential, the parameter n: noticeable differences are only observed in the first maximum of the $P(\theta)$ distribution (at $\theta \simeq 56°$). A piece of

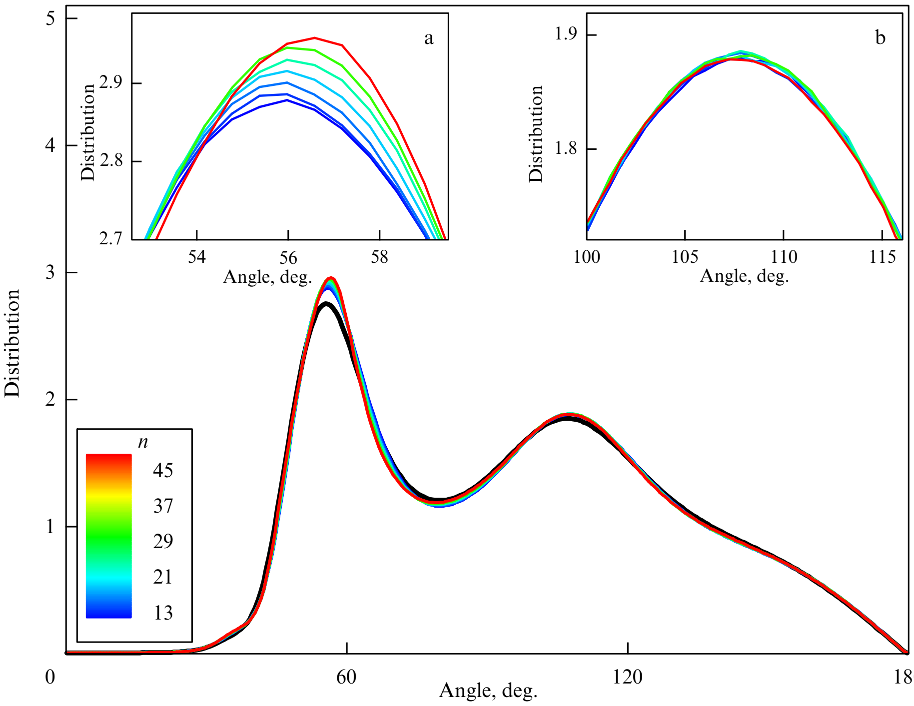

Figure 10. Behavior of the $P(\theta)$ distribution for the melt of a system of soft spheres. BADF functions are given for various values of the exponent n in a range of 10–50, which spans the range of interparticle interaction from soft ($n \sim 10$) to hard spheres ($n \simeq 50$). Color of the curves depends on the parameter n; as it increases, color changes from blue to red. It can be seen that dependence $P(\theta)$ is rather weakly affected by the softness of the potential, parameter n; all dependences virtually coincide; with an increase in n, only the first peak of the $P(\theta)$ distribution (at $\theta \simeq 56°$) grows. A portion of this BADF region is shown in inset (a). Value of the second maximum is $P(\theta) \approx 1.9$ (at $\theta \simeq 108°$) and barely depends on n, due to which it is a universal characteristic of the melt of soft spheres. A detailed view of the second BADF peak is shown in the inset (b). Also, for comparison, dependence $P(\theta)$ for the melt of the Lennard-Jones system is shown (black line). All distributions $P(\theta)$ were calculated using 12 nearest neighbors.

this BADF segment is shown in the inset in Fig. 10a. It can be seen that the value of the first peak increases with parameter n, so this characteristic is a convenient and simple indicator of the softness of the interparticle interaction in the melt (as well as the parameter $g_{\max}$ considered above).

The value of the second maximum of the $P(\theta)$ distribution observed at $\theta \simeq 108°$ is virtually independent of n and is equal to ≈ 1.9. This makes the indicated parameter a quasi-universal characteristic of the melt of soft spheres. A detailed view of the second BADF peak is shown in the inset to Fig. 10b. For comparison, Fig. 10 also shows the dependence $P(\theta)$ for the melt of a Lennard-Jones system. The magnitude of the first BADF peak clearly shows that the interparticle interaction in the LJ system is softer than in the system of soft spheres (for $n > 10$): the value of the first maximum in the $P(\theta)$ distribution is ≈ 2.75 for the LJ melt, while, for the soft sphere, melt (with the parameter $n = 10$) is significantly larger: approximately ≈ 2.9. The value of the second BADF peak for the LJ melt, as in the case of soft sphere melts, is ≈ 1.9, which, in particular, confirms the quasi-universality of this parameter.

Three-dimensional systems with a long-range interaction potential, which include Coulomb systems, soft sphere systems, and Yukawa systems with small values of n and κ, crystallize with the formation of a bcc lattice, which is typical of systems with soft interparticle interaction. As mentioned above, the second coordination sphere in this type of crystal is located not far from the first one, and, under heating, they combine, which greatly complicates the identification of bcc-like crystallites. Therefore, it is of interest to consider how the BADF function changes as the nearest neighbors are moved away from the central atom and, consequently, how the angular correlations of these nearest neighbors change.

Such an example is displayed in Fig. 11, which shows the angular characteristics of the bcc lattice in the crystalline phase and near the melting line of the crystal and liquid. The angular distributions $P(\theta)$ calculated for the nearest 14 neighbors are presented as functions of their distance from the central particle. In Fig. 11a, such dependences are plotted for a bcc crystal at temperature $T \simeq 0{,}3T_{\mathrm{m}}$, where T_{m} is the melting temperature. The presence of two spatially separated coordination spheres is clearly seen. Figures 11c and 11e correspond to a crystal (c) and a liquid (e) near the melting line. In Fig. 11b, d, f, the projections of the nearest 14 neighbors onto the unit sphere are constructed for all considered configurations. The color of the particles changes from blue to red as they move away from the central atom.

Such visualization of nearest neighbors often makes it possible to determine the type of lattice in crystalline clusters, the phase state of the system under study, the presence of anisotropy in it, etc. [56]. For example, an isotropic liquid can be easily distinguished from even a crystal strongly distorted by the thermal motion of atoms, clearly seen if Fig. 11d and 11f are compared. Figure 11 also shows that the fine details of the angular distribution of nearest neighbors virtually disappear under heating to the melting temperature, and both coordination shells spread out in space and unite. This behavior of the coordination shells cannot be revealed using the one-dimensional BADF function; for this, one needs to know how the BADF changes in the radial direction from the central atom, so that the considered 2D angular distribution function is an important structural characteristic of an

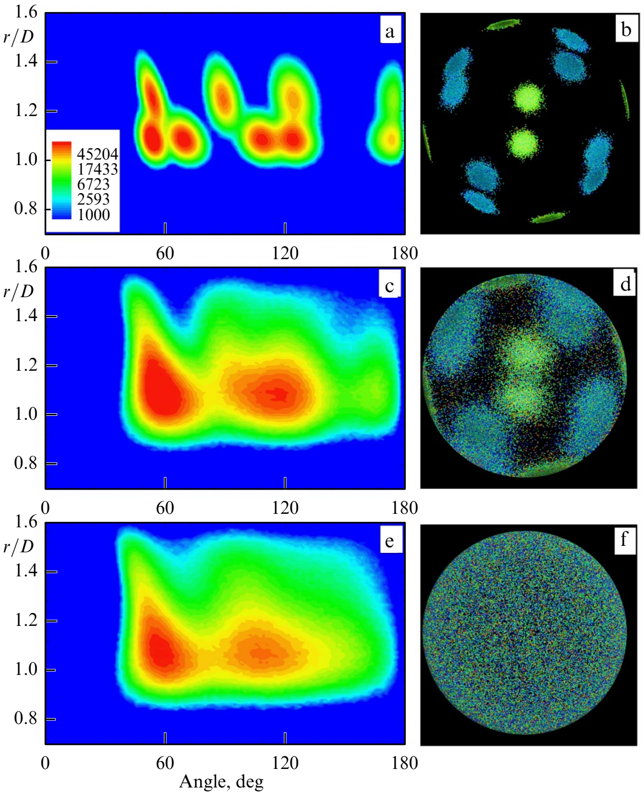

Figure 11. Melting of a 3D Yukawa system with screening parameter $\kappa = 1$, which has a bcc lattice at low temperatures. Left row of panels (a, c, e) shows how the BADF function calculated for the nearest 14 neighbors changes depending on the dimensionless distance r/D to the central particle at various temperatures. Panels on the right (b, d, f) show the projections of the position of the nearest 14 neighbors onto a unit sphere to visualize their distribution in space. Their color, which depends on the distance to the central particle, changes from blue to red as distance increases. Panels a, b correspond to the bcc crystal at temperature $T \simeq 0{,}3T_{\mathrm{m}}$, where T_{m} is the melting temperature of the system. Panels (c, d) and (e, f) are plotted for a crystal and a liquid on the melting line, respectively.

ensemble of particles. However, in many cases, especially in crystallizing systems, when different types of crystallites are formed concurrently, for example, in a system of hard spheres during their compaction [57], the use of BADF-type averaged angular distributions is unproductive. For a more accurate identification of crystalline clusters in such systems, it is necessary to study higher-order angular correlations.

2.4 Method of rotational invariants

To determine the parameters that characterize the local orientational order and contain angular correlations of a higher order than the angular distribution function BADF, it is convenient to use the rotational invariant method (often also referred to as the Bond Orientational Order Parameter method). This method, which was proposed in [58–61], is widely used to quantitatively describe short-range and average orientational orders in various substances: in Lennard-Jones systems [59, 62–65], hard spheres [66–71], colloidal [72–75] and complex (dusty) plasmas [74–80], metallic glasses [2, 83–86], granular systems [87, 88], liquids with anomalous properties [89, 90], etc. It is currently the most reliable method for detecting and identifying crystalline clusters in the condensed phase and determining structural anomalies in complex liquids, since it is very sensitive to the presence of angular correlations among nearest neighbors. Since the role of the computational experiment in the physics of condensed matter is increasing, it will inevitably be used more widely.

In this method, for each ith particle, the number of $N_{\mathrm{nn}}(i)$ nearest neighbors is first determined. The vectors $\mathbf{r}_{ij}$ connecting the ith particle with its nearest neighbors ($j = 1, \ldots, N_{\mathrm{nn}}$) make it possible to find the local orientational parameter $q_{lm}(i)$ for each atom or particle according to

$$q_{lm}(i) = \frac{1}{N_{\mathrm{nn}}(i)} \sum_{j=1}^{N_{\mathrm{nn}}(i)} Y_{lm}(\theta_j, \phi_j)\,, \tag{10}$$

where $Y_{lm}(\theta, \phi)$ are spherical harmonics and θ, ϕ are the angular coordinates of the jth particle determined by the vector $\mathbf{r}_{ij}$.

It should be noted that the local orientational order defined in this way depends on only two parameters: the angular distribution of the nearest neighbors θ_i and ϕ_i; moreover, the nearest neighbors are usually those particles that are located in the first coordination sphere of a given atom. Sometimes, especially if close-packed substances are studied, it is convenient to use a fixed number of nearest neighbors $N_{\mathrm{nn}} = 12$. In identifying crystalline clusters with the bcc symmetry type, it is better to use $N_{\mathrm{nn}} = 14$, for a simple cubic lattice, $N_{\mathrm{nn}} = 6$, for diamond-like lattice, $N_{\mathrm{nn}} = 4$, etc.

For each particle, rotational invariants of the second $q_l(i)$ and third $w_l(i)$ kind are calculated using $q_{lm}(i)$:

$$q_l(i) = \left(\frac{4\pi}{2l+1} \sum_{m=-l}^{m=l} \left|q_{lm}(i)\right|^2\right)^{1/2}, \tag{11}$$

$$w_l(i) = \sum_{\substack{m_1, m_2, m_3 \\ m_1+m_2+m_3=0}} \begin{pmatrix} l & l & l \\ m_1 & m_2 & m_3 \end{pmatrix} q_{lm_1}(i) q_{lm_2}(i) q_{lm_3}(i)\,, \tag{12}$$

where

$$\begin{pmatrix} l & l & l \\ m_1 & m_2 & m_3 \end{pmatrix}$$

are Wigner $3j$-symbols; in the last equation (12), summation is carried out over all indices $m_i = -l, \ldots, l$ that satisfy the condition $m_1 + m_2 + m_3 = 0$.

It is important to note that each type of crystal lattice has its own unique set of rotational invariants q_l and w_l. This makes it possible to determine the ordered structure observed in experiments or in numerical simulation by comparing the values q_l, w_l calculated for each particle with the values of the invariants q_l^{id}, w_l^{id} for ideal lattices. To identify a crystal structure, it is usually sufficient to use rotational invariants of the second kind, q_4, q_6, and the third kind, w_4, w_6, which are easily calculated for ideal crystals. Such rotational invariants for some common types of crystal lattices are given in Table 1.

In the case of a thermal distortion of the lattice, the identification of solid-state clusters often becomes a nontrivial problem; it is especially difficult to determine the bcc lattice distorted by the thermal motion of atoms. In this case, as was shown above, the second shell is often combined with the first one, and the resulting solid structure can be mistaken for the fcc or hcp symmetry types [91]. This issue is discussed in more detail below.

If we consider close-packed crystalline clusters ($N_{\mathrm{nn}} = 12$), then the highest values of the invariant $q_6 \approx 0.66$ are for the

Table 1. Rotational invariants q_l and w_l ($l = 4, 6$) of some ideal crystal structures calculated for a fixed number of nearest neighbors (NN), which are specified for each type of symmetry. Values q_4, q_6, w_4, and w_6 are presented for the following lattices: hexagonal close packing (hcp), face-centered cubic (fcc), icosahedral (ico), body-centered cubic (bcc), face-centered tetragonal (fct), simple hexagonal (sh), simple cubic (sc), and diamond (dia). For bcc, data are presented for the first shell (NN = 8), the first two shells (NN = 14), and NN = 12 (discussed in detail in the text).

Crystal lattice type	q_4	q_6	w_4	w_6
hcp (NN = 12)	0.097	0.485	0.134	−0.012
fcc (NN = 12)	0.19	0.575	−0.159	−0.013
Icosahedral (ico) (NN = 12)	1.4×10^{-4}	0.663	−0.159	−0.169
bcc (NN = 8)	0.5	0.628	−0.159	0.013
bcc (NN = 14)	0.036	0.51	0.159	0.013
bcc_1 (NN = 12)	0.137	0.559	−0.138	0.0043
bcc_2 (NN = 12)	0.1	0.542	−0.089	0.01
fct (NN = 12)	0.225	0.51	0.11	0.018
sh (NN = 8)	0.53	0.5	0.134	0.0475
sc (NN = 6)	0.76	0.35	0.159	0.013
Diamond (dia) (NN = 4)	0.51	0.628	−0.159	0.013

icosahedron, an important structural element of the quasi-crystalline phase in metallic glasses [2, 52] and supercooled liquids. The value of the invariant q_6 is often used to describe the degree of order in a system of particles. This is due to the fact that, for a completely disordered system (gas phase), the average value is $q_6 \simeq 0.29$ (for $N_{\text{nn}} = 12$), while the values of the parameter q_6 for solid-state clusters are much higher.

In the case of the bcc lattice, given its importance and the complexity of identification mentioned above, Table 1 presents rotational invariants not only for the first coordination sphere ($N_{\text{nn}} = 8$) and for the first two spheres ($N_{\text{nn}} = 14$) but also for the case when the number of nearest neighbors $N_{\text{nn}} = 12$. Often, there are systems in which several solid-state phases exist simultaneously (for example, fcc, hcp, and bcc). This situation is often observed, for example, in experiments with the crystallization of complex [82] and colloidal plasmas [74]. In a system of hard spheres near the Bernal limit, fcc and hcp clusters coexist concurrently with an insignificant fraction of the icosahedral phase [71], etc. In such cases, it is convenient from a practical point of view [37, 38] to determine solid-state clusters by calculating rotational invariants with a fixed number of nearest neighbors, which is characteristic of close packing of atoms ($N_{\text{nn}} = 12$).

It can be easily shown [91] that, for an ideal bcc lattice, only two sets of rotational invariants correspond to this case, into which 15 possible combinations of positions of six atoms of the second shell degenerate. It can be shown that the rotational invariants with magnitude $q_6 \approx 0.137$ are present in only three of the 15 possible combinations. These combinations correspond to the configuration of atoms from 12 particles, where two particles from the second shell located opposite each other are missing. Rotational invariants with $q_6 \approx 0.1$ are consequently present in 12 combinations and, as will be shown below, they dominate during heating (and crystallization) of the bcc lattice. This nice effect, which is a consequence of the bcc lattice symmetry, greatly simplifies the search for even highly distorted bcc-like clusters.

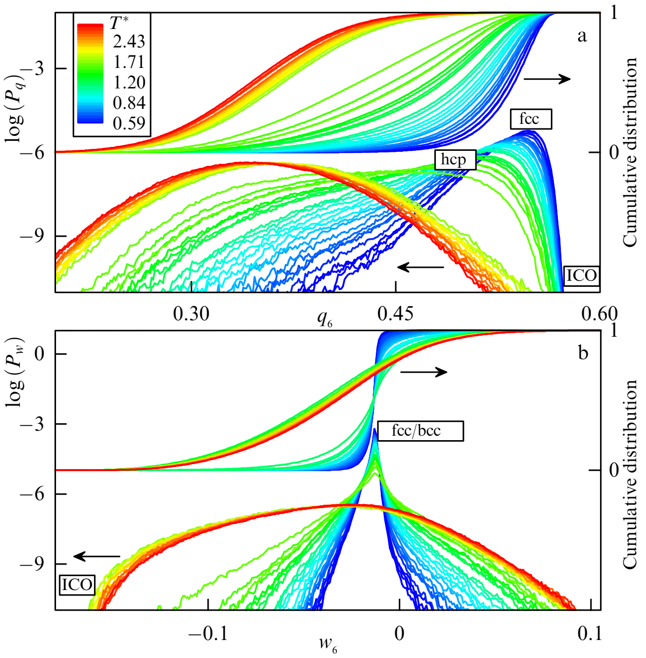

Figure 12. Behavior of rotational invariants near the melting line of a Lennard-Jones system. Distribution functions $P(q_6)$ and $P(w_6)$ normalized to unity are presented, depending on the values of the parameters q_6 (a) and w_6 (b) calculated for 12 nearest neighbors. Corresponding cumulative distributions are also shown (upper curves for each figure). Color of the curves depends on the dimensionless temperature T^* and changes from blue to red as this temperature increases. Distributions are plotted with small constant step δT in temperature ($\delta T \sim 10^{-2} T_{\text{m}}$, where T_{m} is the melting point). Crystal–liquid transition region is clearly visible (manifested by a sharp change in the distance between neighboring curves and a change in their shape). Strong broadening of $P(q_6)$ and $P(w_6)$ distributions is also observed in the crystalline phase near the crystal–liquid transition region. Additionally, values of q_6 and w_6 are shown for ideal crystallites, fcc, hcp, and ico, which can be observed in such close-packed systems.

In a liquid, when an ideal crystal is heated, liquid solidifies, etc., atoms are formed with different values of rotational invariants. Such systems can be characterized by calculating the probability distributions $P(q_l)$ and $P(w_l)$ of finding an atom in the system with given values of the invariant q_l or w_l. As an example, Fig. 12 shows how similar distributions $P(q_6)$ and $P(w_6)$ normalized to unity behave as functions of the rotational invariants q_6 and w_6 during the melting of a Lennard-Jones system [64]. In addition to these distributions, Fig. 12 also shows their cumulative distributions $C_{q,w}$, which were proposed in [82] for a quantitative description of the local orientational order. For example, for the invariant q_6, such a cumulative distribution is defined as the integral characteristic of the distribution $P(q_6)$ from

$$C_q(x) = \int_{-\infty}^{x} P(q_6)\,\mathrm{d}q_6\,. \tag{13}$$

It is apparent that $C_q(x)$ is the fraction in the system of particles whose value of the rotational invariant $q_6 < x$ and $C_q(\infty) \equiv 1$. Such distributions are often much more convenient for practical use than the original distributions $P(q_l)$ and $P(w_l)$, since they are smooth, even in the presence of several types of lattice in the system and vary in the range of 0–1. Additionally, if the cumulative distributions $C_q(x)$ and $C_w(x)$ are known, the fraction of solid-state clusters F_{cr} in the system can be easily estimated, which is determined from the difference

$$F_{\mathrm{cr}} \equiv C_q(x_{\mathrm{cr}} + \delta_{\mathrm{cr}}) - C_q(x_{\mathrm{cr}} - \delta_{\mathrm{cr}})\,, \tag{14}$$

where x_{cr} is the value of the invariant for an ideal crystal, and δ_{cr} is the parameter that determines the permissible accuracy of the change in the rotational invariant, at which a cluster of atoms is still considered a crystallite. Often, to identify crystallites, the parameter δ_{cr} is taken equal to $\delta_{\mathrm{cr}} \simeq x_{\mathrm{cr}}/10$, but this parameter may vary depending on the rotational invariant and lattice type. For example, distorted icosahedrons in metallic glasses [2, 52] retained their pentagonal (five-fold) symmetry at values of the rotational invariant $q_6 \simeq 0.58$, which is much less than the value q_6 for an ideal icosahedron ($q_6^{\mathrm{ico}} \approx 0.66$).

Figure 12 clearly shows the separation of the curves into solid and liquid phases for $P(q_6)$ and $P(w_6)$ and their cumulative distributions. All curves are constructed for the LJ system near the melting line with a constant small step in temperature, so the region of the crystal–liquid transition is very clearly visible from a sharp increase in the distance between adjacent curves and a change in their shape, which is clearly observed from both types of P and C distributions mentioned. However, distributions of the rotational invariant of the third kind w_6 exhibit this transition much more distinctly, i.e., for this invariant, such distributions turn out to be much more sensitive to the destruction of the local orientational order during melting than do those over the invariant of the second kind q_6. This is an important property of the rotational invariant w_6 and the distributions associated with it. For example, a simple indicator of the melting of a Lennard-Jones system (as, notably, can be seen from Fig. 12) is the disappearance of a singularity (sharp peak) in the distribution $P(w_6)$, which is observed at $w_6 \approx w_6^{\mathrm{fcc}}$, i.e., for values of w_6 close to the rotational invariant of an ideal fcc lattice.

Thus, the set of distributions $P(q_i)$ and $P(w_i)$ calculated for the melt of a substance for different invariants q_i and w_i is its important characteristic and, naturally, the question arises as to how universal such distributions are. Figure 13 shows the dependences $P(q_6)$ and $P(w_6)$ and their cumulative functions $C(q_6)$ and $C(w_6)$ obtained for an equilibrium melt of a Lennard-Jones system at two values of the reduced density: $\rho^* = 1$ and $\rho^* = 3.5$. With such a change in density, the melting temperature changes by more than two orders of magnitude, so that the above example covers a significant part of the phase diagram of the LJ system. It can be seen that the presented distributions do not depend on the density of the system (this result is undoubtedly true for intermediate values of density ρ^* in the range of 1–3.5), which, in turn, implies that these distributions are universal characteristics of the LJ melt.

To describe the local orientational order, it is often convenient to deal not with distributions $P(q_i)$, $P(w_i)$, $C(q_i)$, and $C(w_i)$, some of which are shown in Figs 12 and 13, but with a single number that characterizes each such distribution. To this end, it is preferable to use smooth cumulative functions $C(q_4)$, $C(q_6)$, $C(w_6)$, etc., which by construction vary from 0 to 1. In [70, 82], it was proposed to use as such a numerical characteristic so-called cumulants, the values of the rotational invariant at the point where the cumulative function C is equal to 1/2. Then, the cumulant, for example, for the distribution $C(q_6)$, by definition is the number Q_6 determined from the equality

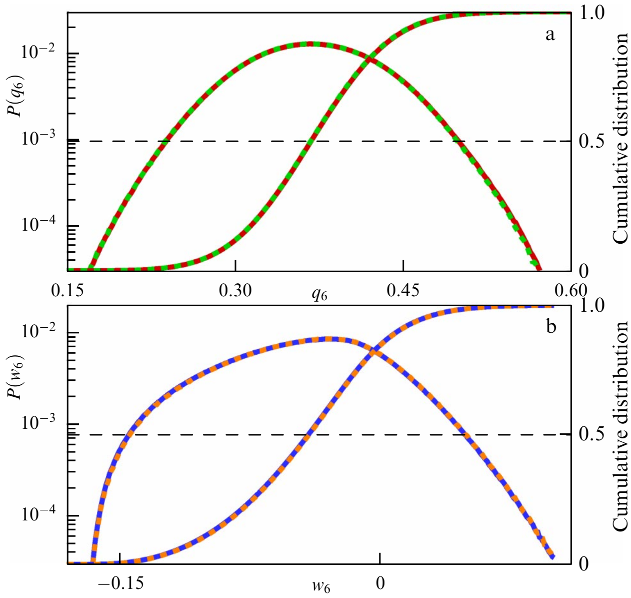

Figure 13. Equilibrium melt of a Lennard-Jones system. Dependences $P(q_6)$ (a) and $P(w_6)$ (b) of the LJ melt are shown along with their cumulative distributions for two values of the reduced density $\rho^* = 1$ (red and blue curves) and $\rho^* = 3.5$ (dashed lines). It can be seen that the considered distributions do not depend on the density of the system in the range $\rho^* \in 1-3.5$, i.e., they are universal characteristics of the LJ melt. The $P(q_6)$ and $P(w_6)$ distributions are calculated taking into account the 12 nearest neighbors.

$$C(Q_6) \equiv \frac{1}{2}\,. \tag{15}$$

The cumulants determined in this way, being calculated for the distributions $C(q_i)$ and $C(w_i)$, turn out to be very sensitive characteristics of structural transformations in matter for various systems [64, 70, 85, 90]. Figure 14 shows, as an example, the variation in the cumulants of distributions $C(q_i)$, $C(w_i)$ (for $i = 4, 6$) near the melting line of a Lennard-Jones system. It can be seen that all the considered cumulants undergo an abrupt change in the process of melting, which is accompanied by the destruction of the local orientational order. The liquid near the melting line is characterized by cumulants that are virtually independent of density ρ^* of the LJ system. This is illustrated by the inset to Fig. 14, which shows the cumulants of the melt as a function of ρ^*. Thus, the proposed cumulants are universal characteristics of the LJ melt, which are suggested here to be used as indicators of the melting of such a system. In Table 2, they are presented in two forms: the top line displays the absolute values of the cumulants Q_4, Q_6, W_4, and W_6 for the LJ melt, while the

Table 2. Universal characteristics of the local orientational order for a Lennard-Jones melt. Cumulants are Q_4, Q_6, W_4, and W_6 (upper line) and the same quantities expressed in units of the invariant of an ideal fcc lattice (lower lines): Q_4/q_4^{fcc}, Q_6/q_6^{fcc}, W_4/w_4^{fcc}, and W_6/w_6^{fcc}.

Cumulant values	Q_4	Q_6	W_4	W_6
LJ melt	0.15	0.37	−0.025	−0.04
LJ melt (in fcc-invariant units)	0.8	0.64	0.15	3
Crystal on the melting line (in fcc-invariant units)	0.93	0.78	0.5	1

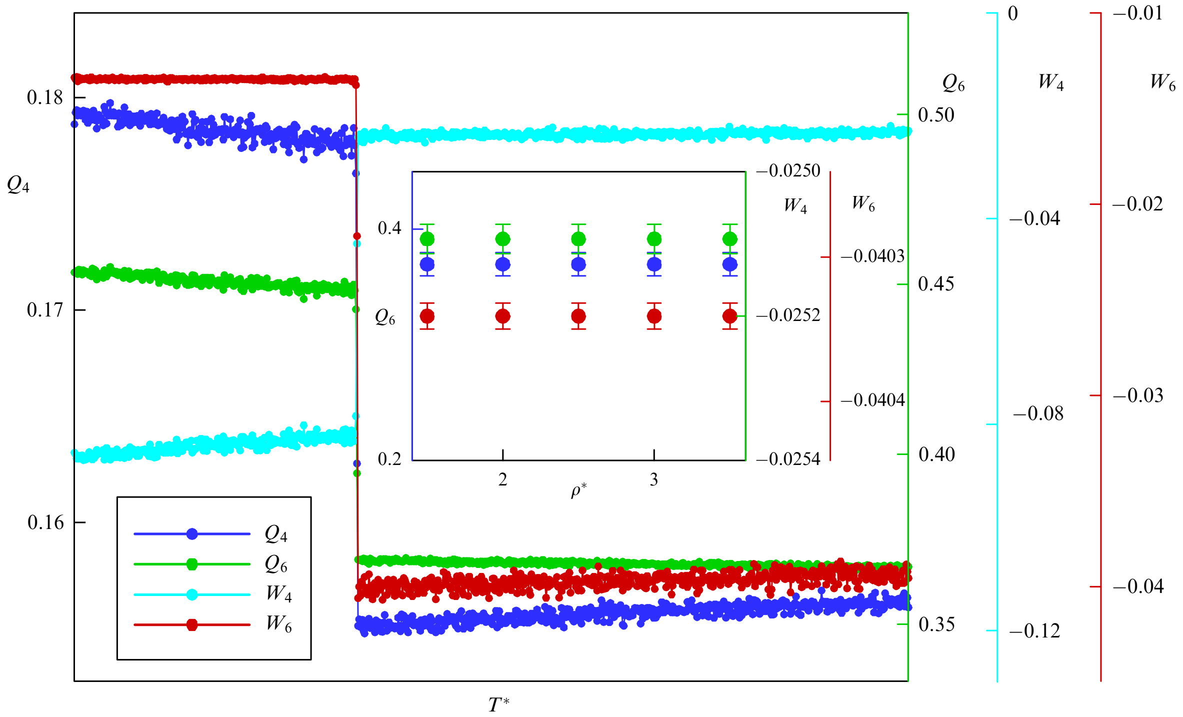

Figure 14. Melting of a Lennard-Jones system. Dependence of cumulants of distributions $C(q_i)$ and $C(w_i)$ (for $i = 4, 6$) on reduced temperature T^* near the melting line. A sharp jump, which is observed for all cumulants, corresponds to the destruction of the local orientational order and the melting of the system. Inset shows dependence of the cumulants Q_6, W_4, and W_6 of the melt on density ρ^*. It is clearly seen that these cumulants are virtually independent of density and, thus, are universal characteristics of the LJ melt.

second line shows the same data, but normalized to the values of the corresponding rotational invariants for the ideal fcc lattice, which is characteristic of crystalline phase LJ systems: Q_4/q_4^{fcc}, Q_6/q_6^{fcc}, W_4/w_4^{fcc}, and W_6/w_6^{fcc}, respectively. Table 2 also shows the normalized cumulants for an fcc crystal on the melting line. The W_6 indicator is probably the most convenient one for practical use.

If, in the same way as Lennard-Jones melts, we analyze the local orientational order for melts of a system with inverse power-law repulsion (IPL) and those of a Yukawa system, it turns out that the distributions $P(q_i)$ and $P(w_i)$ (as well as their cumulative distributions $C(q_i)$, $C(w_i)$) shown in Figs 12 and 13 virtually coincide with the results for these systems provided that the interaction exponent is $n > 8$ and the screening parameter is $\kappa > 5$ (for soft sphere and Yukawa systems with softer interparticle interaction, additional study is required). This, in particular, implies that the universality of the cumulants presented in Table 2 applies to all close-packed systems, from soft to hard spheres.

In other words, it can be argued that all close-packed media (i.e., those systems that feature the fcc or hcp lattice in the crystalline state) melt in the same way in what regards the properties of the local orientational order, i.e., such melts inherit the structural properties of the parent crystal. We also note that the cumulants presented in Table 2 are essentially single-phase melting criteria that can be used to study the melting of close-packed substances. Their accuracy, as can be estimated from the behavior of cumulants near the melting line, is about 1%. Such accuracy is completely inaccessible to other common melting criteria, such as the Lindemann, Verlet, and Hansen criteria.

It should be noted that for a more accurate description of the properties of orientational order in matter using the method of rotational invariants, it is of importance to consider not only one-dimensional distributions $P(q_i)$ and $P(w_i)$ but also 2D ones (for example, the distributions of atoms $P_{2\text{D}}(q_i, w_j)$ on the planes of rotational invariants $(q_4 - q_6)$, $(q_6 - w_6)$, $(w_4 - w_6)$, etc.), 3D distributions $(P_{3\text{D}}(q_i, w_j, w_k))$, etc. This provides a much more detailed description of the pathway of melting and crystallization in the phase space of rotational invariants of various dimensionalities.

Figure 15 shows as an example 2D distributions of particles $P_{2\text{D}}(q_i, w_j)$ on the plane of rotational invariants of the second $(q_4 - q_6)$ (Fig. a) and third kind $(w_4 - w_6)$ (Fig. b) obtained for heated bcc, hcp, and fcc crystals. All invariants are calculated with a fixed number of nearest neighbors $N_{\text{nn}} = 12$ [91]. The rotational invariants for ideal fcc, hcp, and bcc crystals are also shown for comparison with distorted lattices. The absence of noticeable intersections of these distributions makes it possible to reliably identify each type of distorted crystal lattice, despite the significant thermal spread of each of the distributions. This example clearly shows that two-dimensional distributions (and especially a combination of two distributions — on the planes $(q_4 - q_6)$ and $(w_4 - w_6)$) determine the type of crystallite formed in the system under study much more accurately than one-dimensional distributions. Therefore, using rotational invariants, calculated with $N_{\text{nn}} = 12$, and the two-dimensional distributions introduced above (for example, for a crystallizing substance), one can immediately determine the type of crystal lattice which is characteristic of the system under consideration. Additionally, the conclusion made above is confirmed regarding the importance of identifying bcc-like atoms using 12 nearest neighbors to calculate the rotational invariants. Also, Fig. 15b shows that the density at two

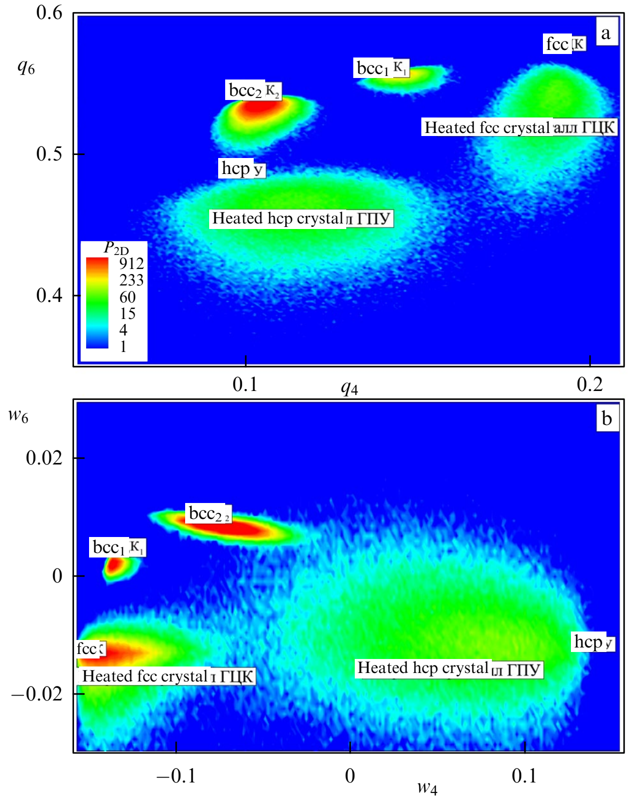

Figure 15. Two-dimensional distributions of particles $P_{2\mathrm{D}}(q_i, q_j)$ on the plane of rotational invariants of the second (q_4-q_6) (a) and third kind (w_4-w_6) (b) for a number of heated crystals: bcc, hcp, and fcc. All invariants are calculated with a fixed number of nearest neighbors $N_{\mathrm{nn}}=12$. Rotational invariants for ideal fcc, hcp, and bcc lattices are also displayed for comparison with the corresponding distorted lattices. In the case of a bcc crystal (see Table 1), the set of 15 possible combinations of four atoms of the second shell degenerates into two sets of invariants (bcc$_1$ and bcc$_2$) of different intensity, which is clearly seen in the presented distributions. Absence of noticeable intersections of these distributions makes it possible to reliably identify each type of distorted crystal lattice, despite their rather significant thermal broadening.

maxima of the 2D distribution for a heated bcc crystal is in good agreement with the degree of their degeneracy — the distribution density in the region of the invariant $q_4 \simeq 0.1$ is several times higher than that of invariant $q_4 \simeq 0.13$.

This observation, in particular, resolves the difficult problem of identifying bcc-like clusters formed during the crystallization of many systems. It can be shown that the calculation of invariants with the number of nearest neighbors $N_{\mathrm{nn}}=8$ and $N_{\mathrm{nn}}=14$ is not very suitable for identifying bcc crystallites: in the first case, they can be easily mistaken for fcc-like clusters, and, in the second case, for fcc- and hcp-like clusters. For a melt of a Lennard-Jones system, the distribution $P_{2\mathrm{D}}^{\mathrm{melt}}(q_4, q_6)$ is shown in Fig. 16. It should be noted that, for the invariant q_6, the maximum distribution ($q_6 \simeq 0.38$) significantly exceeds the average value of the invariant calculated for a fully disordered system ($q_6 \simeq 0.29$). It can also be seen that the melt contains virtually no crystalline clusters; it can be shown that their proportion is exponentially small.

An example of the identification of crystalline clusters using rotational invariants is presented in Fig. 17, where the crystallization of a system of monodisperse hard spheres near the Bernal limit is considered [70, 71]. The most disordered packings of 64,000 hard spheres in a cube with periodic boundary conditions were considered. It is known [57] that in such a system, at a packing density of $\phi \simeq 0.64$, crystalline clusters inevitably appear. Figure 17 shows the spatial distribution of hcp and fcc clusters for three packing densities ϕ: $\phi \approx 0.65$ (a, b), $\phi \approx 0.66$ (c, d), and $\phi \approx 0.68$ (e, f). The color of the particles, which is determined by the crystal cluster size, changes from blue (single cluster) to red as the size increases. It can be seen that for $\phi \approx 0.65$ hcp clusters dominate in the system. For $\phi \approx 0.66$, two types of crystallites are observed: hcp and fcc, which are 3D objects. A further increase in the packing density to $\phi \approx 0.68$ leads to an interesting structural transition: 3D crystalline clusters are transformed into flat layers, forming a layered (sandwich-like) structure, in which layers with fcc symmetry alternate with hcp layers [67]. We note that, just as in the case of melting of close-packed LJ, soft sphere, and Yukawa systems, during the crystallization of a system of hard spheres, the cumulant W_6 undergoes the most dramatic change with the appearance of crystallites [70, 71]. This is due to the practical coincidence of the values of the rotational invariant w_6 for the fcc and hcp lattices.

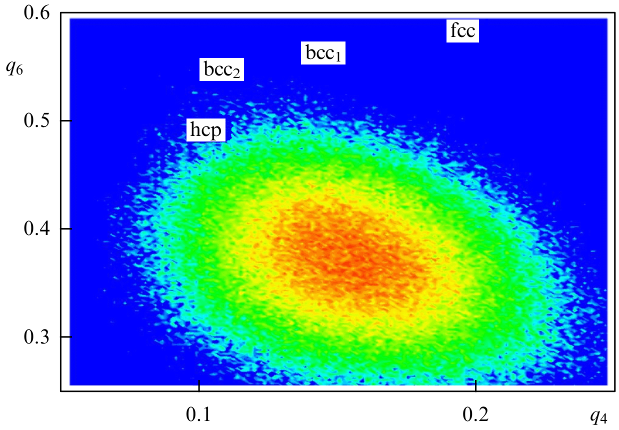

Figure 16. Two-dimensional distribution of particles $P_{2\mathrm{D}}(q_i, q_j)$ on the plane of rotational invariants (q_4-q_6) for a melt of a Lennard-Jones system. For comparison, invariants of ideal lattices are displayed (shown in the figure). The red color corresponds to the maximum distribution density. It can be seen that the melt contains virtually no crystalline clusters: their proportion is exponentially small. All invariants are calculated with a fixed number of nearest neighbors $N_{\mathrm{nn}}=12$.

In concluding this section, we consider a combination of the method of rotational invariants and the Voronoi method. Such an approach was proposed in [49]. In this case, the problem of determining the nearest neighbors is removed: their number N_{nn} for a given atom is simply equal to the number of faces of the Voronoi polyhedron obtained by the VT method. Then, according to [49], in calculating the orientational order parameters $q_{lm}(j)$, the contribution of each neighboring particle j is related to its weight δ_j, which is determined by the area of the Voronoi polyhedron face s_j on which it rests:

$$q_{lm}(i)=\frac{1}{N_{\mathrm{nn}}(i)}\sum_{j=1}^{N_{\mathrm{nn}}(i)}\delta_j Y_{lm}(\theta_j,\phi_j)\,. \tag{16}$$

It is convenient to define $\delta_j = N_{\mathrm{nn}} s_j / S_{\mathrm{tot}}$, where S_{tot} is the area of all faces of a given polyhedron, so $\sum_{k=1}^{N_{\mathrm{nn}}}\delta_k \equiv N_{\mathrm{nn}}$. In this case, the values of the rotational invariants q_l and w_l do not change for ideal fcc, hcp, and ico lattices, since in the above lattices all 12 faces of the corresponding Voronoi polyhedron

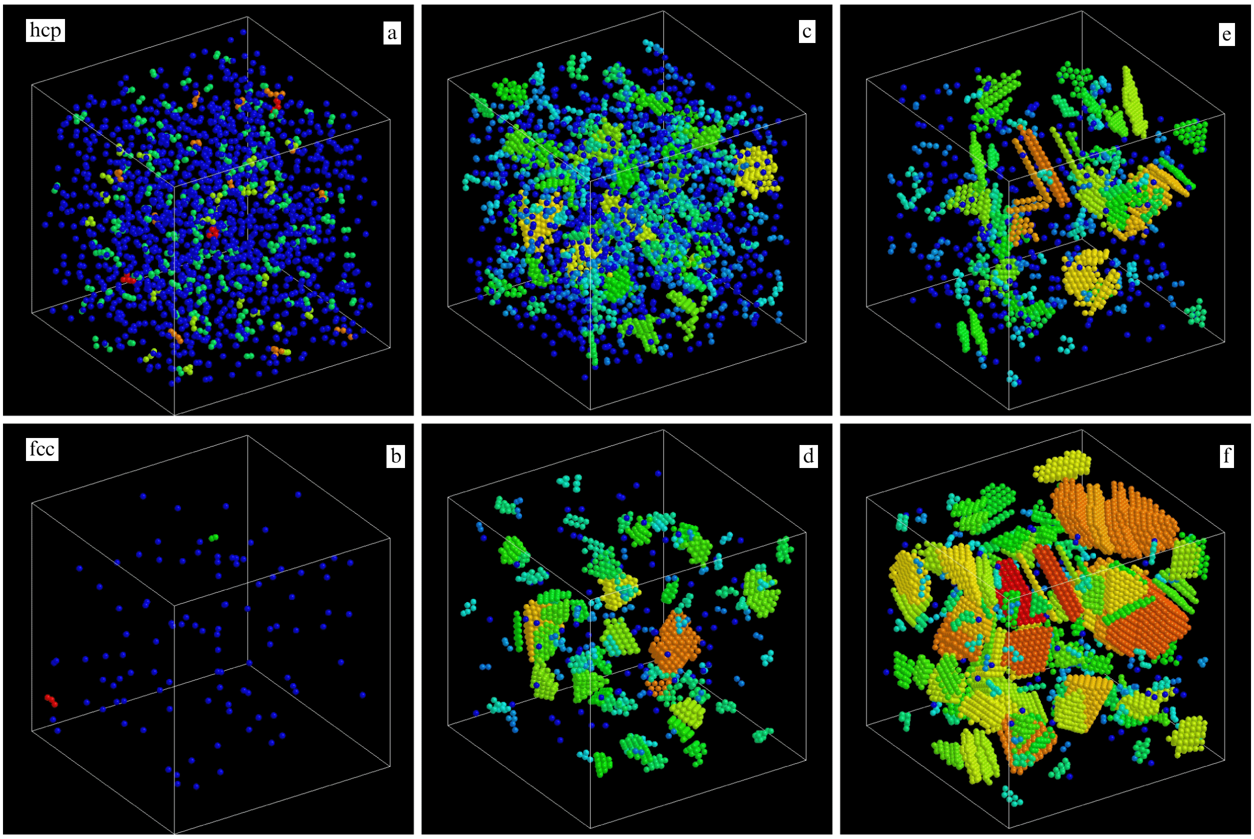

Figure 17. Three-dimensional system of monodisperse hard spheres. Spatial distribution of hcp and fcc clusters is shown for three values of packing density ϕ: $\phi \approx 0.65$ (a, b), $\phi \approx 0.66$ (c, d), and $\phi \approx 0.68$ (e, f). Color of the particles depends on the size of the crystal cluster and changes from blue (single cluster) to red as it increases. For $\phi \approx 0.65$, hcp clusters dominate the system. For $\phi \approx 0.66$, both types of crystallites and hcp and fcc are observed (c, d). A further increase in the packing density results in an interesting structural transition: 3D clusters are transformed into planar, sandwich-like structure (e, f). Number of particles in the system $N = 64 \times 10^3$.

have the same areas. This is not the case for an ideal bcc cluster (smaller faces correspond to 6 particles from the second shell and, consequently, a smaller contribution to q_{lm}). For the case of the fcc lattice, these modified values of the rotational invariants q_4, q_6, w_4, and w_6 are, respectively, 0.224, 0.567, -0.159, and 0.013.

Figure 18 compares two methods for calculating invariants: standard and modified techniques (taking into account the determination of nearest neighbors from the Voronoi partition) using the same atomic configurations. Displayed are two-dimensional distributions $P_{2D}(q_i, q_j)$ of particles on the plane $q_4 - q_6$ for a heated fcc crystal, which was used to calculate the distributions shown in Fig. 15.

Figure 18a corresponds to using the standard approach with a fixed number of nearest neighbors $N_{nn} = 14$. In addition to the bcc lattice invariant, the values of the invariants for ideal fcc and hcp lattices are shown. For the fcc lattice, two sets of invariants are obtained, and, for hcp, three, all of which are shown in the figure. It can be seen, in particular, that all types of considered crystals are present in the given distribution, due to which it is not possible (using only these data) to identify the type of crystallite in the system under consideration.

Figure 18b corresponds to the case when the nearest neighbors for each atom of the distorted bcc lattice were determined by the Voronoi method, and q_{lm} were calculated using Eqn (16). The results are presented for the four most common types of topological clusters in such a system. It is clearly seen that even clusters with Voronoi indices $\langle 0, 6, 0, 8 \rangle$ (which are identical to the indices of the ideal fcc lattice) yield a strong spread in the values of their q_4 and q_6 invariants. For other topological clusters, the scatter is even greater, which implies that this method has no particular advantages in practical application. In [49], the method was tested on a system of close-packed hard spheres; however, in this case, as was shown above, all crystalline clusters are perfectly determined by the standard method of rotational invariants [70, 71].

3. Structure of two-dimensional systems near the crystal–liquid transition

An extensive bibliography is devoted to two-dimensional melting (see, for example, recent detailed review [92] and papers cited there). Two-dimensional systems have been actively studied since the pioneering theoretical works [93–99], which brought in 2016 the Nobel Prize in Physics to D Kosterlitz and D Thouless. The main focus was on the mechanism and properties of the crystal–liquid phase transition in various 2D systems and the physics of formation and the properties of the intermediate (between the crystal and liquid) hexatic phase (characterized, in part, by the presence of a quasi-long-range orientational order and the absence of long-range translational order). A large number of studies have been devoted to the dynamic and structural features of a two-dimensional substance near its melting region [100–105]. In addition, interest in two-dimensional materials and, in particular, in the physical properties of real 2D liquids,

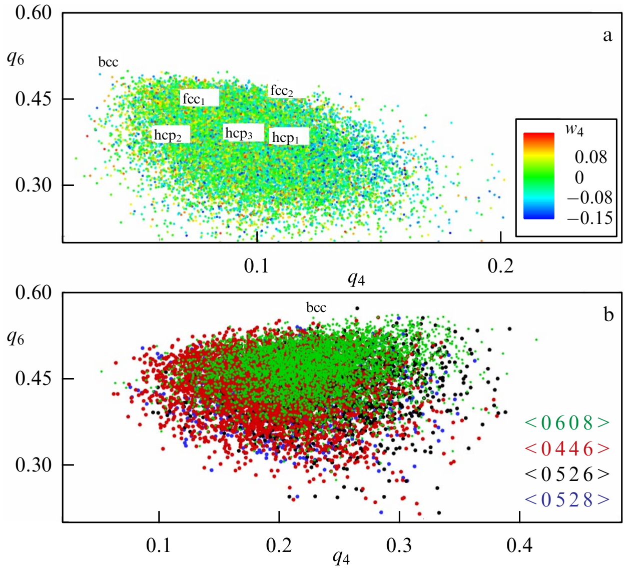

Figure 18. Distributions $P_{2D}(q_i, q_j)$ on the plane of rotational invariants $(q_4 - q_6)$ for a heated bcc lattice. Panel (a) corresponds to the case when the rotational invariants q_4 and q_6 were calculated with a fixed number of nearest neighbors $N_{\rm nn} = 14$. Color of the particles depends on the value of the rotational invariant w_4. Panel (b) shows the same configurations of atoms, but invariants were calculated using Eqn (16). Additionally, panel (a) displays values of invariants for ideal fcc and hcp lattices computed with a fixed $N_{\rm nn} = 14$. For the fcc lattice, this yields two sets of rotational invariants, and for hcp, three sets, all of which are presented in the figure. Panel (b) presents data for the most common topological clusters in such a system (with Voronoi indices, respectively, $\langle 0, 6, 0, 8 \rangle$ (green), $\langle 0, 4, 4, 6 \rangle$ (red), $\langle 0, 5, 2, 6 \rangle$ (black), and $\langle 0, 5, 2, 8 \rangle$ (blue)). Strong broadening of both distributions makes it impossible to determine the type of crystallite by the described methods.

initiated by the discovery of graphene, has recently grown [106, 107]. We also note the recent observation of two-dimensional melting in a system of quasiparticles: skyrmions [108].

Here, we barely touch on the fine details and the type of crystal–liquid transition in the two-dimensional case, and only discuss the structural properties of a 2D liquid using the example of the Yukawa system from the same perspective from which the melts of 3D systems were considered. Note that there are indications that the properties of a liquid near the melting line do not depend on the type of crystal–liquid transition (at least for close-packed systems). Particle configurations, the structural properties of which are considered in this section, were obtained using the method of classical molecular dynamics [13], the characteristic number of particles in the two-dimensional systems under study being $N \sim 10^5$. In the study of the liquid phase, this virtually eliminates the influence of the size of the system on the structure of the liquid.

At zero temperature, the 2D Yukawa system is a close-packed crystal with a triangular (hexagonal) lattice and the number of nearest neighbors for each atom $N_{\rm nn} = 6$, but, at a finite temperature, clusters of defects appear in such a system, in which each particle has $N_{\rm nn} \neq 6$. At low temperatures ($T \ll T_{\rm m}$, where $T_{\rm m}$ is the melting temperature of a two-dimensional crystal), such clusters are dominated by dislocations consisting of defects (5–7) (in which one particle has 5 nearest neighbors and the other has 7) and/or the result of their association, so-called dislocation pairs consisting of four such defects. The formation of single defects (disclinations) (with five or seven nearest neighbors) is also possible, but their concentration in such a system is usually much lower than that of dislocations and dislocation pairs. This is due to the fact that such disclinations create a strong local elastic tension in the system, under which it is energetically favorable for them to convert into a dislocation. Even at low temperatures, the formation of agglomerates from defects is possible, which is conveniently characterized by the number $N_{\rm d}$ of particles with $N_{\rm nn} \neq 6$ that form such an agglomerate. The distribution of such agglomerates depending on $N_{\rm d}$ (i.e., the mass spectrum of clusters of defects) is an important characteristic of a two-dimensional system [82]. It is convenient to include disclinations (point defects with $N_{\rm d} = 1$), dislocations ($N_{\rm d} = 2$), and dislocation pairs ($N_{\rm d} = 4$) in this distribution, calling all objects $N_{\rm d} \geqslant 1$ clusters of defects (CDs).

Figure 19 shows how typical clusters of defects look in different phases of a two-dimensional system (small parts of the system are shown): in a crystal (a), a hexatic phase (c), and a liquid near the melting line (e). The particle configurations shown in Fig. 19a, e, were obtained by simulating the Yukawa system with the screening parameter $\kappa = 3$ and the number of particles in the system $N \simeq 10^5$. The hexatic phase shown in Fig. 19c was obtained in an experiment with colloidal particles [109]. In the case of close-packed systems, such as 2D systems of Lennard-Jones, Yukawa, and soft spheres, the nearest neighbors are easily determined by the Voronoi partition (a two-dimensional analog of the VT method). With such a partition, each particle of the system is associated with a convex polygon, the number of sides of which is equal to the number of nearest neighbors. In Figs 19a, c, e, the color of the particles depends on the number of nearest neighbors: green particles correspond to crystallites (with $N_{\rm nn} = 6$), while blue and red particles correspond to particles with 5 and 7 nearest neighbors, respectively. For each particle configuration, a 2D static structure factor was calculated and shown above each of the considered configurations. A comparison of Fig. 19c and e shows that it is almost impossible to visually distinguish between the hexatic phase and the liquid near the melting line, while it can be done quite easily using the two-dimensional structure factor. This is due to the fact that fine details of the angular distribution of nearest neighbors disappear in a two-dimensional fluid and the structure factor becomes isotropic in the space of wave vectors (see, for example, Refs [110, 111]). The hexatic phase is displayed here to show that 2D melting, which is typically a two-stage process for simple systems (i.e., a crystal–hexatic phase–liquid transition occurs) with different types of phase transitions, is a much more complex process than the melting of 3D systems. Figure 19 also shows the diversity of clusters of defects, even in the case of a 2D crystal (where the CD is not limited to only dislocations and dislocation pairs), which is significantly enhanced in the hexatic phase and melt, for which CDs often consist of large agglomerates with a complex shape. We note that exploration of their role in the melting of 2D systems is only beginning [112].

Similar to the 3D case, to describe a 2D melt, we first consider the behavior of the pair correlation function. In this case, $g(r)$ is determined by the formula

$$g(r) = \frac{1}{N} \left\langle \sum_{j \neq k} \delta\big(r - |\mathbf{r}_j - \mathbf{r}_k|\big) \right\rangle . \tag{17}$$

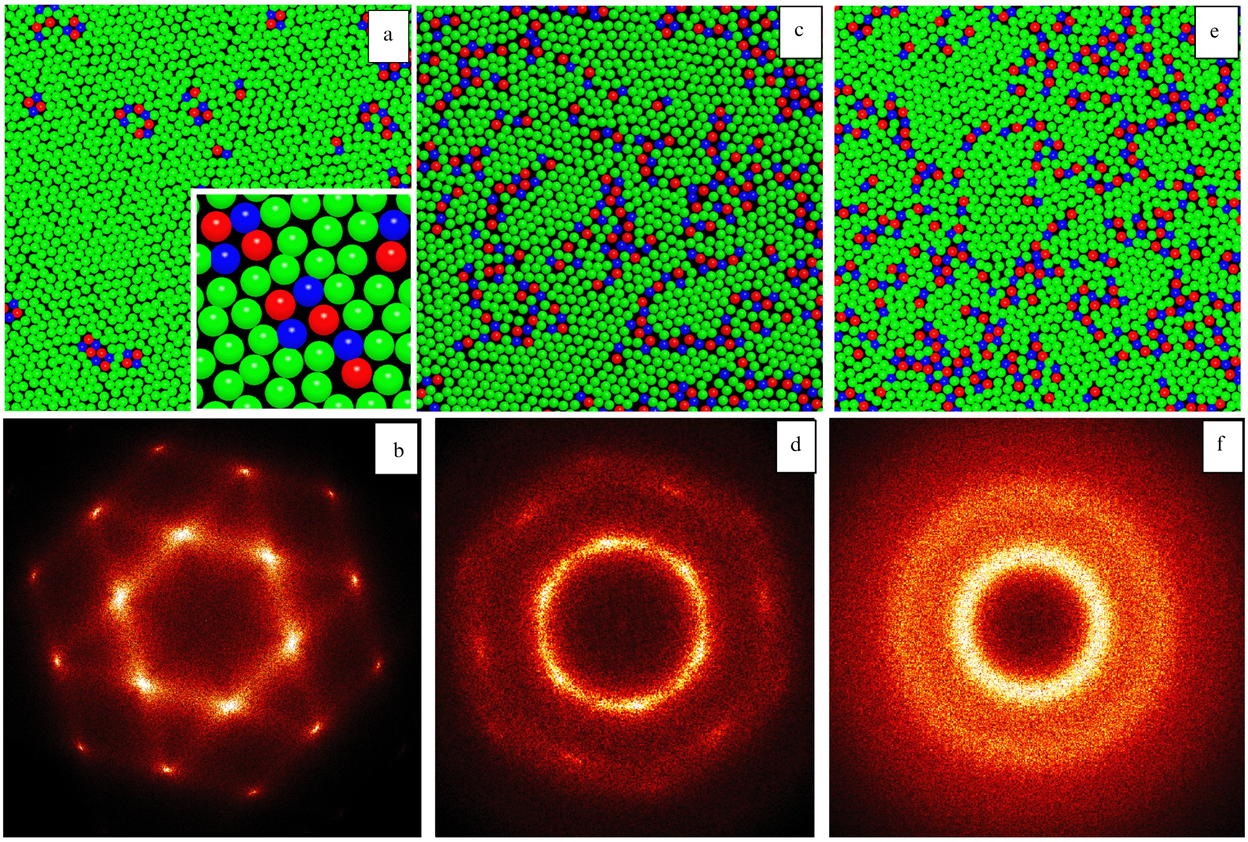

Figure 19. Two-dimensional Yukawa system. Portions of three phases are displayed: crystalline, hexatic, and liquid. Results of numerical simulation of the Yukawa system (with screening parameter $\kappa = 3$) are shown in panels (a) and (d); panel (c) presents the results of an experiment with colloidal plasma [109]. Panel (a) corresponds to the crystalline phase, (e) to the equilibrium liquid near the melting line, and (c) to the hexatic phase. Color of the particles depends on the number of nearest neighbors N_{nn} and changes from blue to red as this number increases. Crystallites with 6 nearest neighbors are highlighted in green, clusters of defects consist of blue and red particles with $N_{\mathrm{nn}} \neq 6$: for blue particles, $N_{\mathrm{nn}} = 5$, for red particles, $N_{\mathrm{nn}} \geqslant 7$. Inset in panel a shows how the most common clusters of defects, dislocations, and dislocation pairs look near the melting line. For each configuration of particles, the corresponding 2D static structure factor (b, d, f) is given below it, which clearly demonstrates structural differences between these phases.

We consider again the characteristics of the PCF, such as its first peak $g_{\max}$ and the first nonzero minimum $g_{\min}$. Their behavior for a melt of a 2D Yukawa system is shown in Fig. 20 for various values of the screening parameter κ [113]. The inset shows the dependences $g(r)$ near the crystal–liquid transition line. The color of the curves depends on the dimensionless temperature $T^* \equiv T/T_{\mathrm{m}}$, where T_{m} is the melting temperature of the system: the blue curves correspond to the crystalline state of the system, and the red curves, to the liquid state. The destruction of the translational order (the disappearance of long-range correlations) during the melting of the system is clearly seen.

The dependences of the parameters $g_{\max}$ and $g_{\min}$ on the value of κ exhibit an interesting effect for melts of the Yukawa system: the PCF $g_{\max}$ peak grows with the increase in the softness of the interparticle interaction (i.e., with an increase in κ), while the parameter $g_{\min}$ does not really change on the melting line in the considered range of variation of the screening parameter and $g_{\min} \approx 0.27$ (for $\kappa \simeq 0-8$). We note that qualitatively the same behavior of the parameters $g_{\max}$ and $g_{\min}$ depending on the softness of the pair interaction was discussed above for three-dimensional melts of a system of soft spheres, which, apparently, reflects a certain structural similarity of melts of close-packed 2D and 3D systems.

Thus, the values $g_{\max}$ and $g_{\min}$ are important characteristics of a 2D liquid, one of which ($g_{\min}$) is a universal indicator of the melting of close-packed systems, while the second ($g_{\max}$) is an indicator of the softness of the pair interaction in the system under study.

In addition, the use of parameters $g_{\max}$ and $g_{\min}$ makes it possible to easily and noninvasively determine the key parameters of pair interaction in 2D experiments with melts of complex and colloidal plasma: the value of $g_{\min}$ is used to determine that the liquid under study is a melt, and the softness of the interaction is found using the parameter $g_{\max}$ (screening parameter κ). For this, a single configuration with the number of particles in the system $N \sim 10^4$ is quite sufficient.

It can be shown that, for a 2D Yukawa liquid at a temperature above the melting point, the value of $g_{\min}$ depends on only one parameter, the dimensionless temperature $T^* = T/T_{\mathrm{m}}$. This is illustrated in Fig. 21, where dependences $g_{\min}(T^*)$ are shown for several values of the screening parameter κ. It is clearly seen that the shape of the curves $g_{\min}(T^*)$ is virtually independent of κ in a wide range of values $\kappa \simeq (0-8)$ and $T^* \simeq (1-2.5)$.

Such properties of the parameter $g_{\min}$ make it possible (together with $g_{\max}$) to determine the location of the 2D Yukawa fluid studied in the experiment (for which the key characteristics of the interaction — the screening parameter κ and the coupling parameter Γ — are usually not known in advance) in the phase diagram, even if such a liquid is located far away from the melting curve: the universality of $g_{\min}(T^*)$ yields the value of T^*, the value of $g_{\max}(T^*)$ can be used to

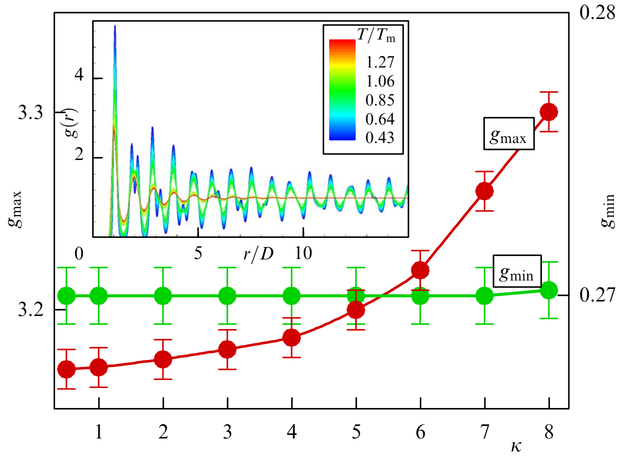

Figure 20. Two-dimensional Yukawa system near the melting line. Dependence of parameters $g_{\max}$ (red line) and $g_{\min}$ (green line) of the melt on the screening parameter κ is displayed. Inset shows the functions $g(r)$ near the crystal–liquid transition line for $\kappa = 3$. Color of the curves in the inset depends on the dimensionless temperature of the system T/T_{m}, where T_{m} is the melting temperature of the 2D Yukawa system. Blue curves correspond to the crystalline state of the system, and red curves, to the liquid state. It is clearly seen that the parameter $g_{\min}$ does not depend on the screening parameter in a wide range of κ values, i.e., this parameter with the value $g_{\min} \approx 0.27$ is a universal characteristic of the 2D melt of the Yukawa system. Parameter $g_{\max}$ increases monotonically with increasing κ in the Yukawa melt, and its value is a simple characteristic of the softness of the interparticle interaction. Number of particles in the system is $N \simeq 10^5$.

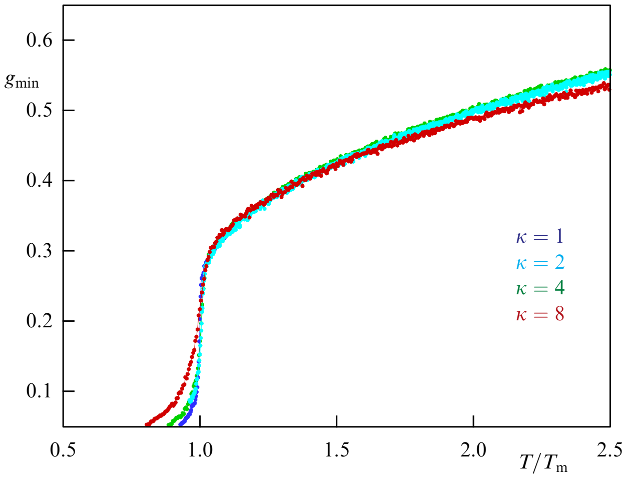

Figure 21. Two-dimensional Yukawa system near the melting line. Dependence of the parameter $g_{\min}$ on the dimensionless temperature $T^* = T/T_{\mathrm{m}}$ for a number of values of the screening parameter κ. Color of the curves depends on the value of κ and changes from blue ($\kappa = 1$) to red ($\kappa = 8$), covering a wide range of interparticle interaction softness. It is clearly seen that, after the crystal–liquid transition (for $T^* > 1$), all the curves virtually coincide, i.e., the value of κ is determined by only the parameter T^*, and the dependence on the screening parameter κ virtually vanishes, at least up to temperatures $T \simeq 2.5T_{\mathrm{m}}$.

find the value of the screening parameter κ, and, knowing κ and the melting curve of the 2D Yukawa system, it is easy to find the temperature of the system T and the coupling parameter Γ.

Integral characteristics $g(r)$, for example, the pair entropy s_2, which describes the contribution of pair correlations to the total entropy [114], and the cumulative pair entropy C_{s2} can also be used to quantitatively describe a 2D fluid [115–118]. The functions s_2 and C_{s2} are defined from

$$s_2 = -\frac{n}{2} \int \big[g(r) \ln g(r) - g(r) + 1 \big] \, \mathrm{d}\mathbf{r} \,, \qquad (18)$$

$$C_{s2}(r) = -\pi \int_0^r \big[g(x) \ln g(x) - g(x) + 1 \big] x \, \mathrm{d}x \,, \qquad (19)$$

where n is the particle density and s_2 is the specific entropy in units of k_{B}. The function $C_{s2}(r)$ shows how quickly the integral in formula (18) converges for 2D systems with increasing distance r, since it is obvious that $C_{s2}(\infty) = s_2$. Similarly to the 3D case, for 2D melts of the Yukawa system, the functions $g(r)$ with different values of the screening parameter κ differ from each other within the first coordination sphere alone; therefore, it should be expected that their integral characteristics will be the same and they can be used as melt characteristics. As an example, Fig. 22 shows the behavior of the dependence of the pair entropy s_2 on the reduced temperature T^* for two values of the screening parameter κ. These curves virtually coincide, which indicates the universality of s_2 as a characteristic of a liquid. The slow decrease in s_2 with increasing temperature for the liquid phase ($T^* > 1$) makes it easy to determine the parameter T^* for the Yukawa fluid under study. A sharp drop in s_2 at $T^* \approx 1$ signals the melting of the system. However, it is not easy to determine from the dependence under consideration the value of pair entropy s_2 which it takes in the melt, since the transition occurs in a narrow temperature range, and a wide range (7–4) of s_2 variation corresponds to a single value of the melting temperature T_{m}. The pair entropy can be determined more precisely by analyzing the convergence of the cumulative entropy C_{s2} to s_2 at large distances. The behavior of C_{s2} as a function of the dimensionless distance r/D and temperature T^* is shown in the inset to Fig. 22 for the parameter $\kappa = 2$. The distance between adjacent curves corresponds to a small ($\delta T^* = 0.01$) temperature step, with the blue lines referring to the crystal, and the red lines, to the liquid. A sharp increase in the distance between neighboring curves corresponds to the melting of the system. The curves plotted on a double logarithmic scale show that in the crystalline phase the cumulative entropy C_{s_2} increases with r and diverges at large distances (and this can be shown by increasing the size of the system). This is related to the presence of a quasi-long-range order in a heated crystal. For liquid, C_{s2} rapidly converges and gives a good estimate of the pair entropy of the melt: $s_2^{\mathrm{m}} \simeq 3.5$. Therefore, for the dependence $s_2(T^*)$ shown in Fig. 22, only the lower part of the curves has physical meaning (at $s_2 < s_2^{\mathrm{m}}$).

It should be noted that the separation of the function C_{s2} into solid and liquid branches (they are shown in Fig. 22) requires a fairly accurate calculation of $g(r)$, which is not always possible in real experiments due to the limited number of configurations of the system under study. A computational experiment does not involve such restrictions, and both characteristics, s_2 and C_{s2}, can be very useful for determining the place of a close-packed liquid in the phase diagram.

In studying the melting of 2D systems, an important role is played by the intermediate hexatic phase, which usually occupies a narrow strip between the crystal and the liquid in the phase diagram. The identification of such a phase is a fairly challenging task. Figure 19 shows that it is very difficult to visually distinguish a hexatic phase from a liquid without a special analysis of the particle configuration. It is usually

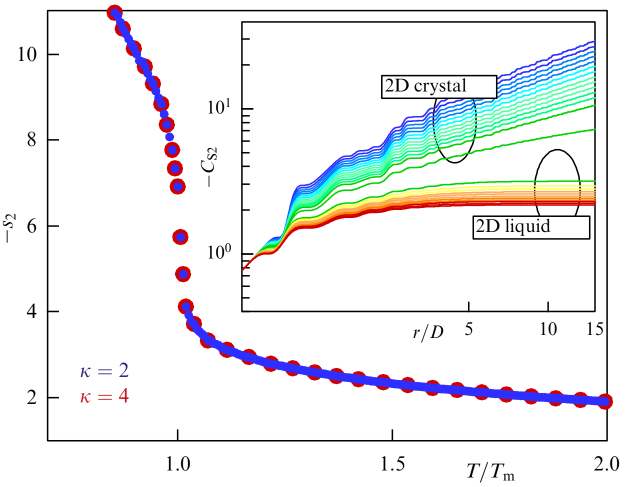

Figure 22. Two-dimensional Yukawa system near the melting line. Pair entropy s_2 is displayed as a function of reduced temperature $T^* = T/T_{\rm m}$ for two values of screening parameter κ. A sharp decrease in s_2 with increasing temperature T^* corresponds to the melting of the system. It can be seen that dependences s_2 are virtually independent of parameter κ and gradually decrease with increasing T^* in the liquid phase ($T^* > 1$). Inset shows the behavior of the cumulative pair entropy $C_{s2}(r)$ for various system temperatures in units of r/D, where D is the average interparticle distance. Temperature varies with a small step $\delta T^* \simeq 0.01$, and a sharp change in the distance between curves corresponds to the melting of the system. Color of the curves depends on temperature T^* and changes from blue to red as it increases, so that the blue color corresponds to the crystalline phase, and the red color corresponds to the liquid phase. Function $C_{s2}(r)$ converges only for the liquid phase. In the melt, $s_2^{\rm m} \simeq 3.5$, so dependence $s_2(T^*)$ has a physical meaning only when $s_2 < s_{\rm m}$.

determined by calculating the orientational correlation function $G_6(r)$ (see, for example, [92]):

$$G_6(r) = \left\langle \frac{\langle \Psi_6(\mathbf{r})\Psi_6(\mathbf{0})\rangle}{g(r)} \right\rangle, \qquad (20)$$

where $\Psi_6(\mathbf{r})$ is a local orientational order parameter determined from

$$\Psi_6(\mathbf{r}_i) = \frac{1}{n_i}\sum_{k=1}^{n_i} \exp\,({\rm i}6\theta_{ik})\,, \qquad (21)$$

where the summation for the ith particle is carried out over all its nearest neighbors n_i, and θ_{ik} is the angle between the vector that connects the ith and kth particles and an arbitrarily directed fixed axis. For a hexagonal ideal lattice, $|\Psi_6(r)| \equiv 1$. In the hexatic phase, $G_6(r)$ decreases with increasing r according to the power law $G_6(r) \propto r^{-\nu_6}$, where $\nu_6 \leqslant 1/4$ (see, for example, [92]). Figure 23 shows the typical behavior of the function $G_6(r)$ near the melting line of the Yukawa system and the orientational correlation functions $G_6(r)$ vs the reduced distance r/D and temperature. During melting, a sharp change in the function $G_6(r)$ occurs: in the crystalline phase, $G_6(r) \approx 1$, while, in the liquid phase $G_6(r) \propto \exp(-r/D)$; both phases are displayed in the figure. The hexatic phase, which is characterized by a quasi-long-range orientational order, is located between them in a narrow temperature range $\Delta T^{\rm hex} \ll T_{\rm m}$.

For finite systems with a relatively small number of particles N (usually $N \sim 10^4$ in real and computational experiments), it is fairly difficult to distinguish the power-law decrease in the correlator $G_6(r)$ from the exponential decrease characteristic of a 2D isotropic fluid (see, for example, [119]). Additional complexity is introduced by the possible metastability of such a phase for finite systems [120]. Therefore, it is important to find simple characteristics of the 2D system that correlate well with the power-law decrease in $G_6(r)$ and are calculable fairly easily.

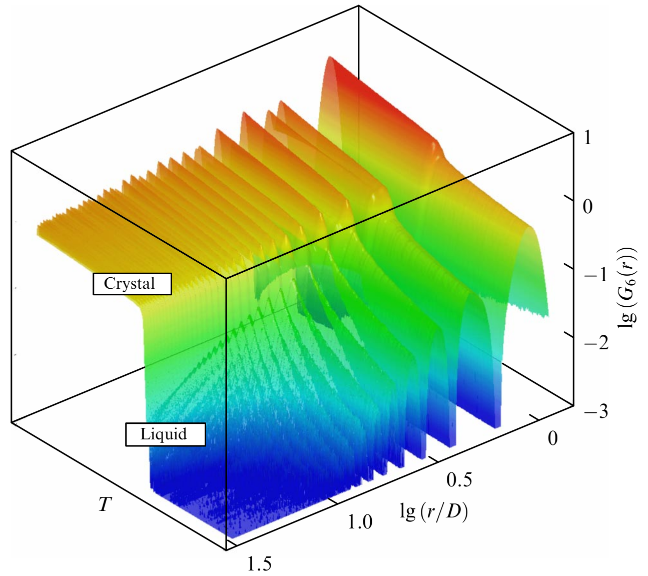

Figure 23. Melting of a 2D Yukawa system with the screening parameter $\kappa = 3$. Orientational correlation functions $G_6(r)$ are presented as functions of the reduced distance r/D and temperature. In the process of melting, a sharp change occurs in function $G_6(r)$, clearly seen in the figure, which shows solid and liquid phases of the system. Hexatic phase characterized by a quasi-long-range orientational order lies between these phases in a narrow temperature range $\Delta T^{\rm hex} \ll T_{\rm m}$. For finite systems with $N \sim 10^4$, finding this phase is not a trivial problem.

The simplest such characteristic of a 2D system is the relative concentration of defective (with $N_{\rm nn} \neq 6$) particles $n_{\rm d} \equiv (1/N)\sum_1^\infty m(N_{\rm d})N_{\rm d}$, where the summation is carried out over all values of $N_{\rm d}$, i.e., over all clusters (consisting of $N_{\rm d}$ particles, each of which has the number of nearest neighbors $N_{\rm nn} \neq 6$), and $m(N_{\rm d})$ is the distribution of such clusters by the number of particles they contain.

Figure 24 shows how the relative concentration $n_{\rm d}$ depends on the reduced temperature of the system $T^* = T/T_{\rm m}$, where $T_{\rm m}$ is the melting temperature. Dependences are presented for two values of the screening parameter: $\kappa = 2$ (blue curve) and $\kappa = 4$ (red curve). It is clearly seen that these curves almost coincide. This implies that the concentration of defects $n_{\rm d}$ does not really depend on the value of the parameter κ in the melting region, i.e., $n_{\rm d}$ is a universal characteristic of the system that depends on only the parameter T^*. This important result makes it possible, in particular, to determine the phase state of the system and the value of the parameter T^* in the experiment, knowing only the concentration of defects, which is rather easily determined from the spatial arrangement of particles by the Voronoi method. For the liquid phase, a similar result has been obtained recently in [113]. A sharp increase in $n_{\rm d}$ observed in a narrow range of reduced temperatures T^* corresponds to the melting of the system with a characteristic value of $n_{\rm d} \simeq 0.2$ for the melt. Insets to Fig. 24 show parts of three phases: crystalline (a) (with $n_{\rm d} \simeq 0.05$), hexatic (b) (with $n_{\rm d} \simeq 0.15$), and liquid (c) ($n_{\rm d} \simeq 0.2$). The color of the

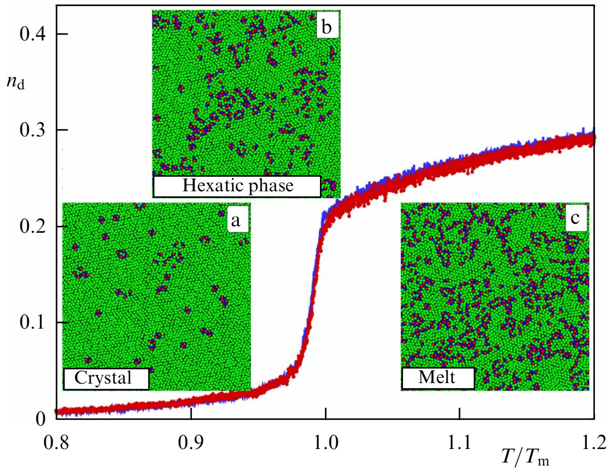

Figure 24. Two-dimensional Yukawa system near the melting region. Relative concentrations n_d of defective particles (i.e., particles with the number of nearest neighbors $N_{nn} \neq 6$) depending on the reduced temperature $T^* = T/T_m$, where T_m is the melting temperature, are shown for two values of the screening parameter: $\kappa = 2$ (blue curve) and $\kappa = 4$ (red curve). These curves almost coincide, which implies that the dependence is quasi-universal in the considered range of T^* values. A sharp increase in n_d, which is observed in a narrow temperature range, corresponds to a crystal–liquid transition with a characteristic value of $n_d \simeq 0.2$ for the melt. Insets show parts of three phases: crystalline (a) ($n_d \simeq 0.05$), thematic (b) ($n_d \simeq 0.15$), and liquid (c) ($n_d \simeq 0.2$). Color of the particles corresponds to the number of nearest neighbors, changing from blue to red as this number increases. It can be seen that parameter n_d is noticeably different for all the specified phases, which enables their identification. Additionally, by determining parameter n_d, one can easily find the reduced temperature of the system T^*.

particles, as in Fig. 19, depends on the number of nearest neighbors: blue and red particles (with five and seven nearest neighbors, respectively) correspond to defective particles, while crystalline particles with six nearest neighbors are highlighted in green. A significant difference between the hexatic and liquid phases and the crystalline one in terms of the type and concentration of defects and clusters of defects greatly simplifies their identification in experiments with complex and colloidal plasma, and the measurement of n_d determines the position of the studied close-packed system on the phase diagram, since it immediately enables an estimation of the parameter T^*.

Analyzing the data of an experiment with a 2D colloidal plasma [109], it can be shown that a power-law decrease in the orientational correlation function $G_6(r)$, which is characteristic of the hexatic phase, is observed at a defect concentration of $n_d \simeq 0.15$. This implies that the parameter n_d is a simple and reliable characteristic of the phase state of 2D close-packed systems. Note that the relative concentration of defects in the melt of the Yukawa system is $n_d \simeq 0.22$, and this result is in good agreement with the data obtained in a numerical experiment for a system of hard spheres [121]. Based on this circumstance, this quantity can be considered an almost universal characteristic of 2D melts in all close-packed systems (i.e., those with a hexagonal lattice at low temperatures), since almost the entire range of interparticle interaction softness — from soft to hard spheres — is spanned.

It is important to note that, in the melts of 2D close-packed systems considered above, about 20% of the particles belong to clusters of defects, and about 80% of the particles belong to crystalline clusters, where each particle has six nearest neighbors. It can be shown [114] that the proportion of such clusters slowly (logarithmically) decreases with increasing temperature, and crystalline particles prevail in the system up to temperatures $T/T_m \sim 30$! This is an important fundamental difference between a 2D liquid and a 3D one (in which the number of crystalline clusters is negligible, even in a melt), which is probably the reason for the complexity of the physics of 2D melting.

In addition to n_d, clusters of defects of various sizes can play an important role in 2D systems [122]. For example, they can be relatively simple parameters characterizing the phase state of a 2D system, as illustrated in Fig. 25, which shows the concentrations of CDs of various masses near the melting region of the 2D Yukawa system. Relative concentrations (fractions) n_N/n_d of clusters consisting of N defective particles are displayed for various temperatures T^*. Dependences are presented for disclinations ($N = 1$), dislocations ($N = 2$), and dislocation pairs and linear clusters (with $N = 4$), as well as for the most common clusters of defects with $N = 3$, $N = 5$, and $N = 6$. Additionally, the cumulative fraction of all defective particles included in clusters of size $N > 4$ is given.

It can be seen that defects — dislocations and clusters with $N = 4$ — dominate in the crystalline phase, although the contribution of other clusters is also quite significant. For example, in a crystal near the melting region, the fraction of CDs (with $N > 4$) is $\simeq 0.3$, which can have a noticeable effect on the melting of this system. At temperature $T^* \leqslant 0.6$, dislocations ($N = 2$) prevail in the system; further, with increasing temperature, clusters consisting of four defects ($N = 4$) start dominating (their fractions become equal: $n_2 \approx n_4$ at $T^* \simeq 0.6$), and their concentration sharply decreases during the crystal–liquid transition. This phenomenon is, in particular, a result of the dissociation of paired dislocations, which, apparently, favors the KTHNY scenario (see, for example, [91]) of such a transition. It is clearly seen that, in both the hexatic phase and the melt, the proportion of relatively large clusters (with $N > 4$) is much higher than in the crystal, and this, most likely, determines the structural and other properties of these phases. The inset to Fig. 25 shows n_d versus T^* on a double logarithmic scale to illustrate the almost power-law growth of n_d in a T^* range of $\simeq 0.6-0.95$ with exponent $\alpha \sim 5$ ($n_d \propto (T^*)^\alpha$). It can be shown that such behavior of a CD near the melting region of the Yukawa system is virtually independent of the screening parameter and, most likely, is typical of close-packed 2D systems.

An important role in the theory of 2D melting is played by paired dislocations, the defects consisting of four defective particles, of which two particles have five and two particles have seven nearest neighbors. They should be distinguished from linear CDs (with $N = 4$). The behavior of both types of CD near the melting region is shown in Fig. 26. The relative concentration n_d of all clusters consisting of four defective particles is shown at various temperatures T^* (blue curve). It is convenient to divide these CDs into two groups, one of which includes paired dislocations, and the other contains linear CDs. They are also shown in Fig. 26 as the fraction of paired dislocations n_{pd} (red curve) and the fraction of linear CDs n_{gb} (green curve). By definition, $n_{pd} + n_{gb} = n_4$. Linear CDs can be easily distinguished from paired dislocations by calculating the maximum distance r_m between particles in the cluster under consideration: for linear CDs it is much larger than for paired dislocations (see the inset to Fig. 26, which shows the distribution of CDs depending on the value of r_m).

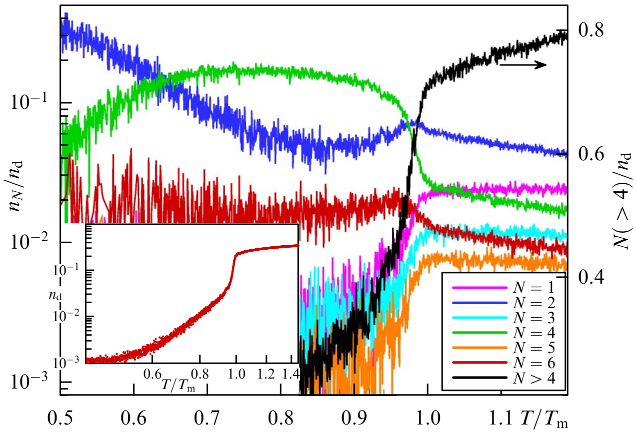

Figure 25. Two-dimensional Yukawa system near the melting region. Relative concentrations n_N/n_d of clusters consisting of N defects are presented as functions of reduced temperature $T^* = T/T_m$. Here, n_d is the concentration of all defective particles in the system (dependence $n_d(T^*)$, which is quasi-universal, is shown in the inset on a double logarithmic scale to illustrate the power-law growth of n_d in the range $T^* \simeq 0.6-0.95$). Different colors show the relative concentrations of defects: disclinations ($N = 1$, purple), dislocations ($N = 2$, blue), and dislocation pairs ($N = 4$, green), as well as clusters of defects with $N = 3$ (turquoise), $N = 5$ (orange), and $N = 6$ (red), respectively. Cumulative fraction of all defective particles in clusters with $N > 4$ is shown in black. It can be seen that defects — dislocations and dislocation pairs — dominate in the crystalline phase, although the contribution of other clusters is quite significant ($\simeq 30\%$ in the crystal near the melting region). At temperatures $T^* \leqslant 0.6$, dislocations ($N = 2$) prevail in the system; subsequently, with increasing temperature, dislocation pairs ($N = 4$) begin to dominate, the concentration of which sharply decreases during the crystal–liquid transition as a result of their dissociation into a pair of dislocations. It is clearly seen that, in the process of melting, the proportion of relatively large clusters (with $N > 4$) sharply increases, amounting to $\simeq 70\%$ in the melt.

It can be seen that paired dislocations significantly dominate in the solid phase; their proportion increases with increasing temperature T^*, while the proportion of linear CDs is very small. In the melting region, the proportion of linear CDs sharply increases and stabilizes in the melt, while the concentration of paired dislocations drops sharply during melting and continues to decrease in the liquid with increasing temperature T^*. This behavior of CDs with $N = 4$ in the melting region can also be used as one of the indicators of the crystal–liquid transition in 2D systems.

The concentrations of defects and clusters of defects n_N provide another important characteristic of a 2D system, the distribution of defects over their 'mass' $P(N)$, which shows which CDs prevail in the system at different stages of its melting and which CDs are most characteristic of a 2D liquid. Such a distribution of clusters of defects $P(N)$ over the number N of defects included in the cluster is shown in Fig. 27 for various temperatures T^* covering all phase states of the 2D Yukawa system. The color of the curves in Fig. 27, which depends on the value of T^*, changes from blue to red as this quantity increases. A sharp increase in the distance between neighboring curves corresponds to the melting of the system. The main properties of these distributions can be seen: in the crystalline phase, $P(N)$ rapidly decreases with increasing N; in the case of a liquid, power-law tails appear in the $P(N)$ dependence, indicating the emergence in the system of large CDs. In addition, the shape of $P(N)$ also changes strongly during melting: the dominance of dislocations and dislocation pairs in the crystalline phase is replaced by a complex spectrum of defect clusters in the hexatic and liquid phases. For not very large values of N, peaks appear in the dependence $P(N)$ that correspond to even values of N. This is a consequence of the kinetics of the formation of various CDs, in which dislocations play a key role.

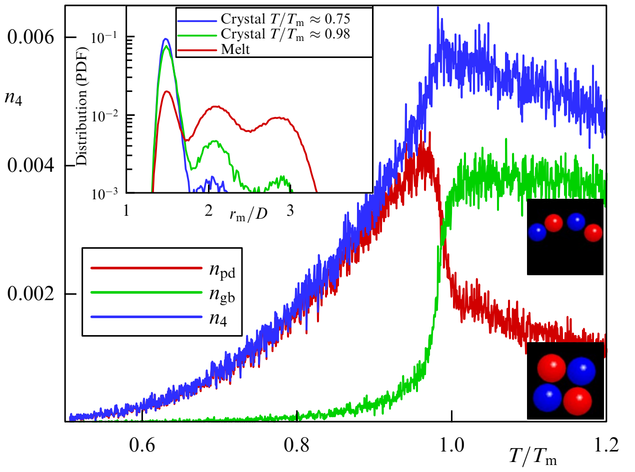

Figure 26. Two-dimensional Yukawa system near the melting region. Relative concentration n_4 of clusters (blue line) consisting of four defective particles near the melting region is displayed as a function of reduced temperature $T^* = T/T_m$. Also shown is the behavior of paired dislocations n_{pd} (red line) and linear n_{gb} defective clusters with $N = 4$ (green line), with $n_{pd} + n_{gb} = n_4$. The characteristic shape of such clusters is also shown. One can see a sharp drop in the concentration of paired dislocations and a sharp increase in linear defective clusters during the melting of the system. Inset shows the distribution of all clusters with $N = 4$ over the maximum distance r_m/D between the particles of which the cluster consists, where D is the average interparticle distance. Such a distribution (shown in the inset for the crystalline phase at various temperatures T^* and for the melt) makes it easy to distinguish paired dislocations from linear defective clusters.

Therefore, more specifically, to describe 2D systems, it is convenient to use a dimensionless parameter defined as the ratio of the concentrations of the two most common CDs, i.e., introduce the parameter $n_{2/4} = n_2/n_4$, which is the ratio of the concentration of dislocations and the concentration of CDs with $N = 4$. The behavior of this parameter for various values of T^* is shown in the inset to Fig. 27. In the crystalline phase near the melting region, $n_{2/4}^{\rm cr} \simeq 0.5$, while for the melt, $n_{2/4}^{\rm m} \simeq 2.5$, and these quantities are virtually independent of screening parameter κ, i.e., are quasi-universal structural characteristics of a 2D melt. Although the structural universalities of melts of 2D systems were considered in this section using as an example the Yukawa system alone, there are reasons to believe that the melts of all close-packed 2D systems feature these universal properties.

In concluding this section, we note that the structure of quasi-two-dimensional systems of microparticles observed in experiments with complex plasma is largely determined by the properties of the external electrostatic potential U_c (confinement) that holds negatively charged microparticles in the center of the gas-discharge chamber. The formation of such a confinement results from fast (compared to ions) diffusion of electrons onto the walls of the discharge chamber. The central region of the high-frequency discharge is positively charged and becomes a potential well for negatively charged microparticles; in the first approximation, it is a parabolic trap ($U_c \propto r^2$) in the plane of a monolayer of microparticles, the

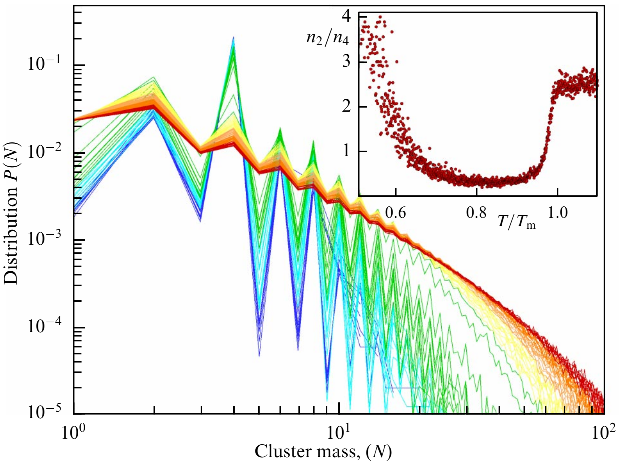

Figure 27. Two-dimensional Yukawa system near the melting region. Distribution of clusters of defects $P(N)$ over number N of defects included in the cluster, calculated for various reduced temperatures T^*. Color of the curves depends on the T^* value and changes from blue to red as this temperature increases. Curves span the range $T^* \simeq 0.8-1.1$ and are constructed in such a way that adjacent curves are associated with a small change in temperature $\delta T^* \sim 10^{-3}$. A sharp increase in the distance between curves corresponds to the melting of the system. It can be seen that, in the crystalline phase, the $P(N)$ distribution rapidly diminishes with increasing N; in the case of the liquid phase, the situation is different: power-law tails appear in the $P(N)$ dependence. In addition, the shape of $P(N)$ changes substantially in the process of melting: the dominance of dislocations and dislocation pairs in the crystalline phase is replaced by a complex spectrum of clusters, in which dislocations and clusters with an even number of defects prevail. Inset shows how the dimensionless parameter $n_{2/4} = n_2/n_4$, defined as the ratio of the concentration of dislocations to the concentration of CDs with $N = 4$, changes when the system is heated. In the crystalline phase near the melting region, $n_{2/4}^{\rm cr} \simeq 0.5$ (at $T^* \approx 0.9$); for a melt, $n_{2/4}^{\rm m} \simeq 2.5$, and these quantities are virtually independent of the screening parameter κ, i.e., are quasi-universal characteristics of a 2D melt.

pair interaction between which is fairly well described by the Yukawa potential.

In such a trap, the radial distribution of particles is fundamentally inhomogeneous: their density decreases monotonically in the radial direction from the center of the system to the periphery [123–128], which, in turn, implies an increase in the local screening parameter κ in the radial direction. Consequently, when a quasi-two-dimensional plasma crystal located in a parabolic confinement is heated, it is its periphery that begins to melt first (where the screening parameter is larger and the melting temperature is correspondingly lower [29]). This leads to a spectacular effect — the formation of a 'melting wave' upon heating of a 2D plasma crystal in such a confinement [127]. This wave is formed on the periphery and propagates towards the center of the system. Moreover, at certain temperatures it is possible to observe a multi-phase system consisting of a crystal (in the central region of a two-dimensional structure), a liquid (on the periphery), and the possible existence of an intermediate hexatic phase. In the processes of the crystallization of a completely molten 2D crystal, a 'crystallization wave' is formed, which (as is apparent from the same considerations) propagates from the center to the periphery of the system. The 'melting wave' effect is well illustrated in Fig. 28, which shows various stages of its formation and propagation discovered in a numerical experiment [127] during heating of a quasi-two-dimensional Yukawa system in a parabolic trap. We expect that this effect will soon be confirmed in future experiments with quasi-two-dimensional complex plasma.

4. Conclusions

Using the example of simple model systems (Lennard-Jones, Yukawa, and systems with inverse power-law repulsion), various structural characteristics of a dense 3D liquid near the melting line of a substance are considered, starting from the poorly studied properties of the pair correlation function to describing the features of the local orientational order in a liquid in terms of rotational invariants. Particular attention was paid to the discussion of simple universal characteristics of the melt, which barely vary along the melting line. The identification of such characteristics can greatly reduce the computational and experimental resources spent on studying the structural and physical properties of a particular substance.

The simplest parameters characterizing the short-range order in matter — the first peak $g_{\max}$ and the first nonzero

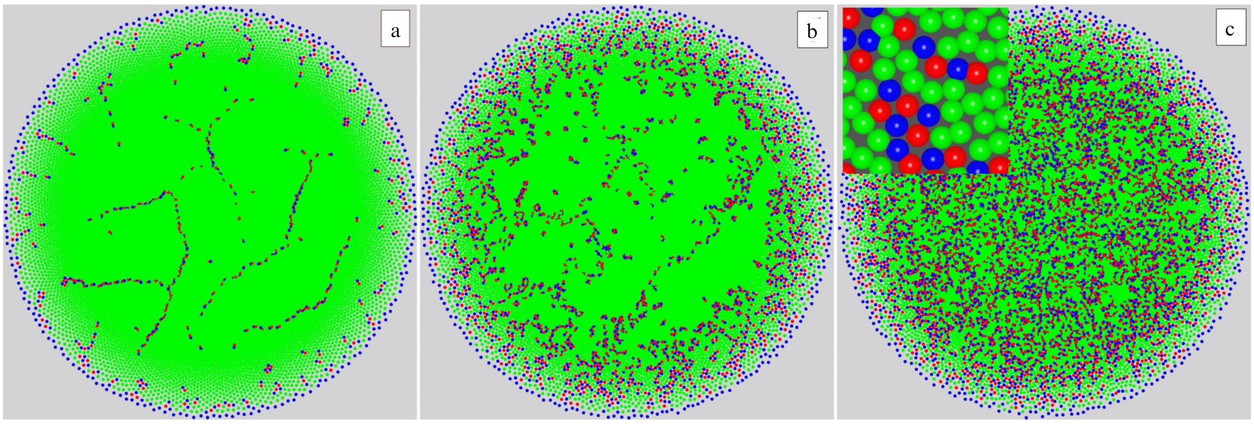

Figure 28. Numerical simulation of a quasi-two-dimensional Yukawa system in parabolic confinement [124]. Characteristic spatial configurations of microparticles are shown at various temperatures T ($T_{\rm a} < T_{\rm b} < T_{\rm c}$). Color of particles, as before, depends on the number of nearest neighbors: green particles represent crystallites; blue and red colors show defective particles with five and seven nearest neighbors, respectively. Panel (a) corresponds to the crystal, (b) is the beginning of the melting of the periphery of the crystal and the formation of a 'melting wave,' which propagates towards its center with increasing temperature, (c) corresponds to the liquid phase, and the inset shows part of the central region of the system.

minimum $g_{\min}$ of the pair correlation function — turn out to be very important characteristics of matter. For melts of close-packed systems, it was found that the value of $g_{\max}$ makes it possible to determine an important property of the melt — the softness of the interparticle interaction. The parameter $g_{\min}$ turned out to be a virtually universal characteristic of the melt with an almost constant value of $g_{\min} \approx 0.55$ for a wide class of systems. For a liquid far from the melting curve, these parameters depend only on the reduced temperature T/T_{m}, which, notably, solves the issue of the place of the liquid under study in the phase diagram. This conclusion is of importance for applications: it is sufficient to know the form of the pair correlation function, which is quite easily determined in the experiment. This is true for a wide class of model systems (from ultrasoft (like Coulomb systems) to hard spheres), but the area of applicability of the results obtained is not limited to these systems.

In studying melts of real substances, it is extremely useful to know their model analog, which has the same values of the parameters $g_{\max}$ and $g_{\min}$ as the liquid under study. Such Yukawa-like or IPL-like analogs of real melts are important for practical applications, since they make it possible to use the characteristics of well-studied model systems to explain the physical properties of real melts observed in experiments. This is especially important in studying systems at very high pressures, when the matter is compressed so strongly that the interparticle interaction is dominated by repulsion, which can always be described by the IPL and/or Yukawa potentials. For melts of simple metals and a number of two-component systems (such as CuZr), the parameter is $g_{\max} \simeq 2.4-2.7$, which makes it possible to classify them as rather soft systems with the exponent of the IPL analog $n \simeq 7 \div 10$. In this context, it would be extremely interesting to find real materials with very stiff interaction (with $n \sim 25$ or $\kappa \simeq 25$); such substances are a rare example of a strongly correlated but weakly coupled system.

Determining the features of the short and medium orientational orders in a liquid is one of the important issues in condensed matter physics, which is currently a challenging problem for a full-scale experiment. Such features are usually studied in a numerical experiment by the methods of quantum and classical molecular dynamics. The simple three-point correlator BADF, which is related to the average angular distribution of the nearest neighbors, and the function $g(r)$ determine two parameters important for the quantitative description of the fluid: the first and second maxima of the mentioned distribution. The first BADF peak is associated with the softness of the pair interaction in the liquid, and the second peak is a universal characteristic of the melt: for close-packed systems, the value of this peak is $\simeq 1.9$ and is virtually independent of the interaction softness.

Significantly more accurate indicators of melting are obtained by using rotational invariants that describe the local orientational order in matter at the local level: for each atom of the system, its own set of invariants is calculated, taking into account its nearest neighbors. Such an approach makes it possible, for example, to easily find liquid (disordered) and crystalline clusters in the system under study. In addition, rotational invariants are much more sensitive to any structural changes in matter than are, for example, the functions $g(r)$ and BADF. The local orientational order in a liquid near the melting line, being described using rotational invariants, exhibits the universality of $P(q_i)$ and $P(w_i)$ distributions for a wide class of close-packed systems, and the cumulants of these distributions are universal melt characteristics. It is convenient to use the cumulant W_6 as an indicator of the melting of such systems, since it is the most sensitive indicator of structural changes in the substance. For the melts of the systems we have considered, $W_6 = 3$, implying that all close-packed systems melt in the same way in what regards the properties of their local orientational order.

The melting of 2D close-packed systems also reveals a number of universal characteristics that do not depend on the softness of the interparticle interaction and are convenient and simple indicators of a 2D melt. The fundamental difference between 2D close-packed systems and 3D systems is that, in 2D melts, about 80% of the atoms are in the form of crystallites (which are virtually absent in melts of 3D systems). This circumstance largely determines the physics of a 2D liquid.

Acknowledgments
The author is grateful to A Z Patashinski for numerous discussions of the issues discussed in this review. The study was supported by the Russian Foundation for Basic Research as part of the Ekspansiya project, no. 20-12-50159.

References

1. Yang Y et al. *Nature* **592** 60 (2021)
2. Hirata A et al. *Science* **341** 376 (2013)
3. Lindemann F *Phys. Z.* **11** 609 (1910)
4. Hansen J-P, Verlet L *Phys. Rev.* **184** 151 (1969)
5. Raveché H J, Mountain R D, Streett W B *J. Chem. Phys.* **61** 1970 (1974)
6. Gnan N et al. *J. Chem. Phys.* **131** 234504 (2009)
7. Hansen J P, McDonald I R *Theory of Simple Liquids* 3rd ed. (Amsterdam – Boston, MA: Elsevier. Academic Press, 2007)
8. Hansen J-P, Schiff D *Mol. Phys.* **25** 1281 (1972)
9. Agrawal R, Kofke D A *Mol. Phys.* **85** 23 (1995)
10. Hamaguchi S, Farouki R T *J. Chem. Phys.* **101** 9876 (1994)
11. Dubin D H E, O'Neil T M *Rev. Mod. Phys.* **71** 87 (1999)
12. Hamaguchi S, Farouki R T, Dubin D H E *Phys. Rev. E* **56** 4671 (1997)
13. Plimpton S *J. Comput. Phys.* **117** (1) 1 (1995)
14. Weber T A, Stillinger F H *Ann. New York Acad Sci.* **371** 335 (1981)
15. Belashchenko D K *Phys. Usp.* **56** 1176 (2013); *Usp. Fiz. Nauk* **183** 1281 (2013)
16. Belashchenko D K *Phys. Usp.* **63** 1161 (2020); *Usp. Fiz. Nauk* **190** 1233 (2020)
17. Saija F, Prestipino S, Guaquinta P V *J. Chem. Phys.* **124** 244504 (2006)
18. Khrapak S, Klumov B, Couëdel L *Sci. Rep.* **7** 7985 (2017)
19. Dyre J C *J. Phys. Chem. B* **118** 10007 (2014)
20. Ingebrigtsen T S, Schrøder T B, Dyre J C *J. Phys. Chem. B* **116** 1018 (2012)
21. Costigliola L, Schrøder T B, Dyre J C *Phys. Chem. Chem. Phys.* **18** 14678 (2016)
22. Zhakhovskii V V *J. Exp. Theor. Phys.* **78** 871 (1994); *Zh. Eksp. Teor. Fiz.* **105** 1615 (1994)
23. Ryltsev R E, Chtchelkatchev N M *Phys. Rev. E* **88** 052101 (2013)
24. Prestipino S, Saija F, Guaquinta P V *J. Chem. Phys.* **123** 144110 (2005)
25. Brazhkin V V et al. *Phys. Rev. E* **85** 031203 (2012)
26. Brazhkin V V et al. *Phys. Usp.* **55** 1061 (2012); *Usp. Fiz. Nauk* **182** 1137 (2012)
27. Brazhkin V V *Phys. Usp.* **62** 623 (2019); *Usp. Fiz. Nauk* **189** 665 (2019);
28. Fortov V E et al. *Phys. Usp.* **47** 447 (2004); *Usp. Fiz. Nauk* **174** 495 (2004)

29. Fortov V E, Morfill G E (Eds) *Complex and Dusty Plasmas*: *From Laboratory to Space* (Boca Raton, FL: CRC Press–Taylor and Francis, 2010)
30. Fortov V E et al. *Phys*. *Rep*. **421** 1 (2005)
31. Morfill G E, Ivlev A V *Rev*. *Mod*. *Phys*. **81** 1353 (2009)
32. Bonitz M, Henning C, Block D *Rep*. *Prog*. *Phys*. **73** 066501 (2010)
33. Nefedov A P, Petrov O F, Fortov V E *Phys*. *Usp*. **40** 1163 (1997); *Usp*. *Fiz*. *Nauk* **167** 1215 (1997)
34. Nefedov A P et al. *New J*. *Phys*. **5** 33 (2003)
35. Mitic S et al. *Phys*. *Rev*. *Lett*. **101** 125002 (2008)
36. Khrapak S A et al. *Phys*. *Rev*. *Lett*. **106** 205001 (2011)
37. Khrapak S A et al. *Phys*. *Rev*. *E* **85** 066407 (2012)
38. Khrapak S A, Klumov B A *Phys*. *Plasmas* **27** 024501 (2020)
39. Minakov D V, Levashov P R *Phys*. *Rev*. *B* **92** 224102 (2015)
40. Voronoi G *J*. *reine angew*. *Math*. **1908** (134) 198 (1908) https://doi.org/10.1515/crll.1908.134.198
41. Finney J L *Proc*. *R*. *Soc*. *Lond*. *A* **319** 479 (1970)
42. Brostow W et al. *Phys*. *Rev*. *B* **57** 13448 (1998)
43. Larsen P M, Schmidt S, Schiøtz J *Modelling Simul*. *Mater*. *Sci*. *Eng*. **24** 055007 (2016)
44. Cheng Y Q, Ma E *Prog*. *Mater*. *Sci*. **56** 379 (2011)
45. Peng H L et al. *Appl*. *Phys*. *Lett*. **96** 021901 (2010)
46. Huang L, Wang C Z, Ho K M *Phys*. *Rev*. *B* **83** 184103 (2011)
47. Chen M *NPG Asia Mater*. **3** 82 (2011)
48. Richard P et al. *Europhys*. *Lett*. **48** 415 (1999)
49. Mickel W et al. *J*. *Chem*. *Phys*. **138** 044501 (2013)
50. Debenedetti P G, Stillinger F H *Nature* **410** 259 (2001)
51. Hirata A et al. *Nat*. *Mater*. **10** 28 (2011)
52. Klumov B A, Ryltsev R E, Chtchelkatchev N M *JETP Lett*. **104** 546 (2016); *Pis'ma Zh*. *Eksp*. *Teor*. *Fiz*. **104** 568 (2016)
53. Klumov B A, Ryltsev R E, Chtchelkatchev N M *J*. *Chem*. *Phys*. **149** 134501 (2018)
54. van Meel J A et al. *J*. *Chem*. *Phys*. **136** 234107 (2012)
55. Xiao F, Yin X *Comput*. *Math*. *Appl*. **72** 328 (2016)
56. Pustylnik M Y et al. *Phys*. *Rev*. *Res*. **2** 033314 (2020)
57. Bernal J D *Proc*. *R*. *Soc*. *Lond*. *A* **280** 299 (1964)
58. Steinhardt P J, Nelson D, Ronchetti M *Phys*. *Rev*. *Lett*. **47** 1297 (1981)
59. Steinhardt P J, Nelson D R, Ronchetti M *Phys*. *Rev*. *B* **28** 784 (1983)
60. Mituś A C, Patashinskii A Z *Phys*. *Lett*. *A* **87** 179 (1982)
61. Mitus A C, Patashinskii A Z *Phys*. *Lett*. *A* **98** 31 (1983)
62. ten Wolde P R, Ruiz-Montero M J, Frenkel D *J*. *Chem*. *Phys*. **104** 9932 (1996)
63. Errington J R, Debenedetti P G, Torquato S *J*. *Chem*. *Phys*. **118** 2256 (2003)
64. Klumov B A *JETP Lett*. **97** 327 (2013); *Zh*. *Eksp*. *Teor*. *Fiz*. **97** 372 (2013)
65. Klumov B A *JETP Lett*. **98** 259 (2013); *Pis'ma Zh*. *Eksp*. *Teor*. *Fiz*. **98** 296 (2013)
66. Torquato S, Truskett T M, Debenedetti P G *Phys*. *Rev*. *Lett*. **84** 2064 (2000)
67. Luchnikov V et al. *J*. *Mol*. *Liq*. **96–97** 185 (2002)
68. Anikeenko A V, Medvedev N N *Phys*. *Rev*. *Lett*. **98** 235504 (2007)
69. Jin Y, Makse H A *Physica A* **389** 5362 (2010)
70. Klumov B A, Khrapak S A, Morfill G E *Phys*. *Rev*. *B* **83** 184105 (2011)
71. Klumov B A, Jin Y, Makse H A *J*. *Phys*. *Chem*. *B* **118** 10761 (2014)
72. van Blaaderen A, Wiltzius P *Science* **270** 1177 (1995)
73. Gasser U et al. *Science* **292** 5515 (2001)
74. Kawasaki T, Tanaka H *J*. *Phys*. *Condens*. *Matter* **22** 232102 (2010)
75. Wochner P et al. *Proc*. *Natl*. *Akad*. *Sci*. *USA* **106** 11511 (2009)
76. Morfill G E et al. *Phys*. *Scr*. **2004** (T107) 59 (2004)
77. Klumov B A, Morfill G E *JETP Lett*. **90** 444 (2009); *Pis'ma Zh*. *Eksp*. *Teor*. *Fiz*. **90** 489 (2009)
78. Klumov B A, Morfill G E *J*. *Exp*. *Theor*. *Phys*. **107** 908 (2008); *Zh*. *Eksp*. *Teor*. *Fiz*. **134** 1059 (2008)
79. Mitic S et al. *Phys*. *Rev*. *Lett*. **101** 125002 (2008)
80. Klumov B et al. *Plasma Phys*. *Control*. *Fusion* **51** 124028 (2009)
81. Klumov B et al. *Europhys*. *Lett*. **92** 15003 (2010)
82. Klumov B A *Phys*. *Usp*. **53** 1053 (2010); *Usp*. *Fiz*. *Nauk* **180** 1095 (2010)
83. Xu R et al. *Nat*. *Mater*. **14** 1099 (2015)
84. Yang L et al. *Scr*. *Mater*. **63** 879 (2010)
85. Ryltsev R E et al. *J*. *Chem*. *Phys*. **145** 034506 (2016)
86. Sheng H W et al. *Nature* **439** 419 (2006)
87. Baule A et al. *Rev*. *Mod*. *Phys*. **90** 015006 (2018)
88. Hanifpour M et al. *Phys*. *Rev*. *Lett*. **113** 148001 (2014)
89. Fomin Yu D et al. *J*. *Chem*. *Phys*. **141** 034508 (2014)
90. Vasilyev O A, Klumov B A, Tkachenko A V *Phys*. *Rev*. *E* **88** 012302 (2013)
91. Klumov B A *JETP Lett*. **114** 406 (2021); *Pis'ma Zh*. *Eksp*. *Teor*. *Fiz*. **114** 467 (2021)
92. Ryzhov V N et al. *Phys*. *Usp*. **60** 857 (2017); *Usp*. *Fiz*. *Nauk* **187** 921 (2017)
93. Berezinskii V L *Sov*. *Phys*. *JETP* **32** 493 (1971); *Zh*. *Eksp*. *Teor*. *Fiz*. **59** 907 (1970)
94. Berezinskii V L *Sov*. *Phys*. *JETP* **34** 610 (1972); *Zh*. *Eksp*. *Teor*. *Fiz*. **61** 1144 (1971)
95. Kosterlitz J M, Thouless D J *J*. *Phys*. *C* **6** 1181 (1973)
96. Halperin B I, Nelson D R *Phys*. *Rev*. *Lett*. **41** 121 (1978)
97. Nelson D R, Halperin B I *Phys*. *Rev*. *B* **19** 2457 (1979)
98. Young A P *Phys*. *Rev*. *B* **19** 1855 (1979)
99. Chui S T *Phys*. *Rev*. *B* **28** 178 (1983)
100. Bedanov V M, Gadiyak G V, Lozovik Yu E *Phys*. *Lett*. *A* **109** 289 (1985)
101. Zahn K, Lenke R, Maret G *Phys*. *Rev*. *Lett*. **82** 2721 (1999)
102. Gasser U et al. *ChemPhysChem* **11** 963 (2010)
103. Wang Z et al. *J*. *Chem*. *Phys*. **132** 154501 (2010)
104. Kapfer S C, Krauth W *Phys*. *Rev*. *Lett*. **114** 035702 (2015)
105. Hartmann P et al. *Phys*. *Rev*. *E* **72** 026409 (2005)
106. Zakharchenko K V, Katsnelson M I, Fasolino A *Phys*. *Rev*. *Lett*. **102** 046808 (2009)
107. Los J H *Phys*. *Rev*. *B* **91** 045415 (2015)
108. Huang P et al. *Nat*. *Nanotechnol*. **15** 761 (2020)
109. Lin B-J, Chen L-J *J*. *Chem*. *Phys*. **126** 034706 (2007)
110. Krebs Z et al. *J*. *Chem*. *Phys*. **149** 034503 (2018)
111. Sun X et al. *Sci*. *Rep*. **6** 24056 (2016)
112. Digregorio P et al. *Soft Matter* **18** 566 (2022)
113. Klumov B A *JETP Lett*. **115** 108 (2022); *Pis'ma Zh*. *Eksp*. *Teor*. *Fiz*. **115** 117 (2022)
114. Baranyai A, Evans D J *Phys*. *Rev*. *A* **40** 3817 (1989)
115. Wang Z et al. *J*. *Chem*. *Phys*. **134** 034506 (2011)
116. Thorneywork A L et al. *Phys*. *Rev*. *Lett*. **115** 268301 (2015)
117. Thorneywork A L et al. *J*. *Phys*. *Condens*. *Matter* **30** 104003 (2018)
118. Klumov B A, Khrapak S A *Results Phys*. **17** 103020 (2020)
119. Ryzhov V N et al. *Phys*. *Usp*. **63** 417 (2020); *Usp*. *Fiz*. *Nauk* **190** 449 (2020)
120. Derzsi A et al. *Phys*. *Plasmas* **21** 023706 (2014)
121. Qi W, Gantapara A P, Dijkstra M *Soft Matter* **10** 5449 (2014)
122. Klumov B A *JETP Lett*. **116** 703 (2022); *Pis'ma Zh*. *Eksp*. *Teor*. *Fiz*. **116** 681 (2022)
123. Dubin D H E *Phys*. *Rev*. *E* **55** 4017 (1997)
124. Totsuji H, Totsuji C, Tsuruta K *Phys*. *Rev*. *E* **64** 066402 (2001)
125. Sheridan T E *Phys*. *Plasmas* **16** 083705 (2009)
126. Durniak C et al. *IEEE Trans*. *Plasma Sci*. **38** 2412 (2010)
127. Klumov B A *JETP Lett*. **110** 715 (2019); *Pis'ma Zh*. *Eksp*. *Teor*. *Fiz*. **110** 729 (2019)
128. Syrovatka R A et al. *JETP Lett*. **116** 869 (2022); *Pis'ma Zh*. *Eksp*. *Teor*. *Fiz*. **116** 836 (2022)